



## Hexagonal BN- and BNO-supported Au and Pt nanocatalysts in carbon monoxide oxidation and carbon dioxide hydrogenation reactions



Andrey M. Kovalskii<sup>a,\*</sup>, Ilia N. Volkov<sup>a</sup>, Nikolay D. Evdokimenko<sup>a,b</sup>, Olga P. Tkachenko<sup>b</sup>, Denis V. Leybo<sup>a</sup>, Ilya V. Chepkasov<sup>d</sup>, Zakhar I. Popov<sup>c,h</sup>, Andrei T. Matveev<sup>a</sup>, Anton Manakhov<sup>a</sup>, Elizaveta S. Permyakova<sup>a</sup>, Anton S. Konopatsky<sup>a</sup>, Alexander L. Kustov<sup>a,b,e</sup>, Dmitri V. Golberg<sup>f,g</sup>, Dmitry V. Shtansky<sup>a,\*</sup>

<sup>a</sup> National University of Science and Technology "MISIS", Leninskiy prospect 4, Moscow 119049, Russian Federation

<sup>b</sup> Institute of Organic Chemistry RAS, Leninskiy prospect 47, Moscow 119991, Russian Federation

<sup>c</sup> Emanuel Institute of Biochemical Physics RAS, Kosygina 4, Moscow 119334, Russian Federation

<sup>d</sup> Skolkovo Institute of Science and Technology, Bolshoy Boulevard 30, bld. 1, Moscow 121205, Russian Federation

<sup>e</sup> Moscow State University, GSP-1, Leninskie Gory, Moscow 119991, Russian Federation

<sup>f</sup> Centre for Materials Science and School of Chemistry and Physics, Queensland University of Technology (QLD), 2 George str., Brisbane, QLD 4000, Australia

<sup>g</sup> World Premier International Center for Materials Nanoarchitectonics (WPI-MANA), National Institute for Materials Science (NIMS), Namiki 1–1, Tsukuba, Ibaraki 3050044, Japan

<sup>h</sup> Plekhanov Russian University of Economics, 36 Stremyanny per., Moscow 117997, Russian Federation

### ARTICLE INFO

#### Keywords:

Au/h-BN(O) and Pt/h-BN(O) nanohybrids  
Carbon dioxide hydrogenation  
Carbon monoxide oxidation  
Catalytic activity  
Hexagonal BN

### ABSTRACT

Environmental protection requires solving the problem of utilization and reduction of CO and CO<sub>2</sub> emissions. Herein, Au/h-BN(O) and Pt/h-BN(O) nanohybrids are thoroughly analyzed in CO oxidation and CO<sub>2</sub> hydrogenation reactions. The nanohybrids differ in catalytic particle size and particle distribution. The particles are smaller (1–6 nm) and display a narrower size distribution in the case of Pt-based nanomaterials. The Pt/h-BN(O) nanohybrids exhibit high catalytic activity in CO conversion and carbon dioxide hydrogenation reactions. For both systems, the oxidative state of BN support affects the catalytic activity. The possible catalytic reaction mechanisms are proposed based on DFT calculations. A charge density distribution at the Pt/h-BN interface increases oxygen absorption, thereby accelerating oxygen-associated chemical reactions.

### 1. Introduction

The on-going development of industrial technologies and associated growth in the production and consumption of energy resources have made a significant contribution to improving the quality of life, but this is accompanied with strong environmental pollution by CO and CO<sub>2</sub> gases. The most effective ways to utilize and reduce their emissions are CO oxidation and CO<sub>2</sub> hydrogenation based on heterogeneous catalysis. Depending on the processing conditions and the nature of catalyst, reduction of CO<sub>2</sub> with hydrogen produces either CO, which is a valuable raw material for several chemical syntheses, or CH<sub>4</sub>. Noble metals are used in many industrial catalytic processes and they are able to dissociate molecular oxygen even at low temperatures and bind strongly to atomic oxygen and CO. These are important characteristics of effective catalysts [1–3].

Noble metal-based catalysts have shown high efficiency in CO oxidation reaction in the production of high-purity hydrogen for fuel cells via selective oxidation in the process of steam reforming, partial catalytic oxidation, and autothermal reforming of liquid fuels and hydrocarbons [4,5]. Gold (Au) and platinum (Pt) nanoparticles (NPs) are well known as effective low temperature catalysts. Therefore, the production of dispersed supported noble metal NPs is of great interest for heterogeneous catalysis [6–8]. Au and Pt catalysts are used in chemical industry for processing hydrocarbons and polymer production [9]. Noble metal NPs-based catalysts have been commercially developed and used in systems for gas purification from CO, including gas masks [10].

The properties of various catalytic systems strongly depend on a support of catalytically active materials [11]. Such support can affect various chemical reactions while accelerating some and slowing down or even stopping the others. The support can change the dispersion of

\* Corresponding authors at: National University of Science and Technology "MISIS", Leninskiy prospect 4, Moscow 119049, Russian Federation

E-mail addresses: [andreykovalskii@gmail.com](mailto:andreykovalskii@gmail.com) (A.M. Kovalskii), [shtansky@shs.misis.ru](mailto:shtansky@shs.misis.ru) (D.V. Shtansky).

catalytically active NPs and their thermal stability by forming chemical bonds with the active material. This prevents nanoparticle agglomeration and changes the chemical properties of the active material through chemical bonds polarization. In recent years, hexagonal boron nitride (*h*-BN), which can be obtained in various morphologies with a high specific surface area, has been regarded as a promising support material. It has been shown that defects in *h*-BN structure (B and N vacancies, as well as N atoms substituted by B atoms) contribute to the dissociation of hydrogen molecules [12]. The chemisorption of CO molecules on *h*-BN defects can be accompanied by a charge transfer and can lead to narrowing of the band gap [13]. BN surface defects result in the polarization of electron density in the catalytically active particles, thereby improving their functional characteristics [14,15]. Theoretical investigations indicate that metal atoms interact with *h*-BN surface defects; this prevents their aggregation [16]. Moreover, metal atoms embedded into *h*-BN surface effectively activate CO molecules. This leads us to consider that a metal/*h*-BN system could be a potentially effective catalyst for carbon monoxide oxidation.

Experimental and theoretical studies have also shown that the morphologies of catalyst and support both affect the reactivity of oxygen and the metal-support interactions. This is manifested in the catalyst activity. For example, it has been shown that the shape and size of catalyst NPs and nanostructured features of the support can significantly affect the oxygen activity, which is explained by different types of defects and the presence of isolated or clustered vacancies [17]. It has also been demonstrated that the adsorption of CO<sub>2</sub> changes depending on the crystallographic orientation of the catalytically active NPs; this affects the desorption of the final products and conversion of CO [18].

Available data indicates that the usage of *h*-BN as a support can increase the catalyst activity compared to commonly used supports. Due to their layered structure, *h*-BN nanosheets enable a high-density attachment of metal NPs leading to an enhanced catalytic activity [19–21]. As a result of redistribution of electron density, defect-free *h*-BN surface possesses catalytic activity under interactions with metal NPs [22]. The presence of vacancy defects over *h*-BN surface can additionally enhance metal-support interaction via electron donor/acceptor mechanisms [23]. This can significantly improve the activity of a catalyst.

Theoretical studies have shown a high efficiency of metal nanoparticle catalysts supported on *h*-BN nanostructures in CO oxidation process [14,24]. BN had usually been considered as a chemically inert material until its unusual behavior was discovered during catalysis. Catalytic activity of pure *h*-BN nanosheets was explained by the presence of oxygen-terminated “armchair” BN edges that act as catalytic active sites [25]. Due to high oxidation resistance of *h*-BN, it is difficult to form B-O active sites at the “armchair” edges during oxidative dehydrogenation. C-H activation to form B-O(H) active sites has been proposed to explain this mechanism [26].

A study of molecular adsorption energy on the surface of support and catalytically active phase made a great contribution to understanding the catalyst efficiency. The dissociations of small molecules onto graphene, *h*-BN, BN-doped graphene, and C-doped *h*-BN using density functional theory (DFT) were studied and a significant difference in dissociative adsorption energies of H<sub>2</sub>, methane, water, and methanol on the surface of these materials was documented [27]. Doping of pristine *h*-BN with carbon atoms increases the adsorption energies of molecules, wherein the reactivity toward non-polar adsorbates increases even more significantly.

In this study, Au and Pt NPs on the surface of two types of *h*-BN nanosheets (reduced and oxidized) were fabricated and thoroughly analyzed as promising catalysts in carbon monooxide oxidation and carbon dioxide hydrogenation reactions. Oxygen activation mechanisms and metal-support interactions are then discussed. The obtained materials are considered as universal catalysts in the CO oxidation and CO<sub>2</sub> hydrogenation reactions.

## 2. Experimental

### 2.1. Catalyst synthesis

#### 2.1.1. Catalyst support fabrication

BN nanoparticles were produced via plasma-chemical synthesis using boron trichloride (“Plazmotherm”, Russia). The nanoparticle size was 20–50 nm. The particles were organized in stacks made of 10–15 atomic BN layers. The specific surface area of BN nanoparticles measured by the BET method was 203 m<sup>2</sup>/g. The obtained material was purified from the possible secondary phases under annealing at 1500 °C for 2 h in vacuum. This type of BN nanoparticles is denoted as BNNPs. The half of annealed BNNPs was subjected to a mild surface oxidation by exposure to air at 1100 °C for 2 min (hereafter denoted as BNNPsOx).

#### 2.1.2. Au/*h*-BN nanohybrids fabrication

BNNPs and BNNPsOx powders were separately dispersed in polyethylene glycol 400 (PEG, Mw=400) for 2 h using an ultrasonic bath. Then, without interrupting sonication, chloroauric acid (HAuCl<sub>4</sub>·nH<sub>2</sub>O) water solution was added dropwise to the nanoparticle suspensions to achieve two different Au contents, ~4 and ~8 wt%. The mass fraction of Au in chloroauric acid aqueous solution was 18 g/l. The resulting suspensions were sonicated in an ultrasonic bath without additional cooling over 12 h. During processing, the temperature of suspensions reached 57 °C and they acquired a characteristic dark purple color, which indicates a nanometric Au particle size [28]. The resulting suspensions were washed with distilled water and then centrifugated at 9000 rpm. These procedures were repeated 10 times.

#### 2.1.3. Pt/*h*-BN nanohybrids fabrication

BNNPs and BNNPsOx powders were dispersed in distilled water under ultrasonic treatment, first in an immersible sonotrode unit for 5 min, and then in an ultrasonic bath for 2 h. An external water flow was used to cool the suspension during processing. Pt/BN(O) nanohybrids were obtained via impregnation method from the hexachloroplatinic acid (H<sub>2</sub>PtCl<sub>6</sub>·6 H<sub>2</sub>O). The mass fraction of Pt in hexachloroplatinic acid aqueous solution was 10 g/l. After preliminary sonication for 2 h, the aqueous hydrofluoric acid solution was added directly during the ultrasonic treatment to achieve 4 wt% of Pt and then the homogenization was carried out for another 2 h. The obtained suspensions were evaporated on a magnetic stirrer under constant stirring. Dried mixtures were heat-treated at 350 °C in Ar (80 cm<sup>3</sup>/min) and H<sub>2</sub> (20 cm<sup>3</sup>/min) flow for 3 h until complete reduction of Pt on the surface of BN nanoparticles was accomplished.

## 2.2. Catalytic tests

### 2.2.1. Carbon monoxide oxidation

Carbon monoxide oxidation reaction was executed using a ChemBET Pulsar instrument (Quantachrome). Catalytic properties of the metal/BNNPs and metal/BNNPsOx nanomaterials and pure BNNPs were analyzed by defining the parameters of CO oxidation in a fixed-bed continuous-flow reactor at the atmospheric pressure as described elsewhere [20].

Pretreatment of catalysts was carried out in a 36 ml/min gas flow (10% H<sub>2</sub> / 90% He) at 350 °C for 1 h. The catalytic tests were conducted in a 36 ml/min flow of gaseous mixture (5.6 mol.% of CO, 11.1 mol.% of O<sub>2</sub>, 83.3 mol.% of He). GHSV = 43.2 L×g<sub>cat</sub><sup>-1</sup> ×h<sup>-1</sup>.

The reaction products were detected using a Thermostar GSD 320 quadrupole mass spectrometer (Pfeiffer Vacuum). CO conversion was calculated using the following equation:

$$\alpha = 1 - \frac{f_{CO}^{out}}{f_{CO}^{in}}$$

where  $f_{CO}^{out}$  is the CO gas flow rate after the catalyst bed and  $f_{CO}^{in}$  is the

initial CO gas flow rate.

### 2.2.2. Carbon dioxide hydrogenation

Carbon dioxide hydrogenation reaction was carried out in a flow-through catalytic unit equipped with a straight stainless steel reactor with an internal diameter of 4 mm with a fixed catalyst layer. 42 mg of catalysts was mixed with 1.2 g of quartz particles. Catalyst on quartz inside the reactor was fixed with two quartz wool plugs (top and bottom). The temperature was measured using a chromel-alumel thermocouple located in the lower part of the catalyst layer. Samples in the reactor were pre-activated in a hydrogen flow at a rate of 50 ml/min. During activation stage, the samples were first heated to a temperature of 500 °C at a rate of 10 °C/min and then maintained at this temperature for 60 min. Finally, the catalyst was cooled to room temperature in a hydrogen flow. The initial CO<sub>2</sub> and H<sub>2</sub> flows were set to 7 and 14 ml/min, respectively. GHSV was 30 L × g<sub>cat</sub><sup>-1</sup> × h<sup>-1</sup>. The pressure was raised up to 30 atm. During the measurement, the reactor was heated at a rate of 10 °C/min. The catalyst sample was kept at the experimental temperature until the equilibrium was reached, that is, until the quantity and composition of the products remained constant over time (at least over 2 h). Then, the measurements were conducted and heating proceeded to the next temperature point at the same rate. The products of carbon dioxide hydrogenation were investigated using a chromatographic method on a CRYSTAL 5000 device equipped with three thermal conductivity detectors, a flame ionization detector, packing columns M ss316 NaX 80/100 mesh 2 m × 2 mm, HayeSep R 80/100 mesh 1 m × 2 mm, M ss316 HayeSep Q 80/100 mesh 2 m × 2 mm and a capillary column MXT® - Alumina BOND/MAPD 30 m × 0.53 mm.

The specific reaction rate was calculated as:

$$r = \frac{(n(CO_2)_{start} - n(CO_2)_{fin})}{m_{cat}}$$

where  $n(CO_2)_{start}$  - molar CO<sub>2</sub> flow (mol/h) at the inlet of reactor,  $n(CO_2)_{fin}$  - mole CO<sub>2</sub> flow (mol/h) after the reactor,  $m_{cat}$  - mass (kg) of the catalyst.

### 2.3. Material characterization

The morphologies of BNNPs and BNNPsOx and as-synthesized metal/BN(O) nanohybrids, were investigated using a scanning electron microscope JSM-7600 F (JEOL) equipped with an EDX detector. Powder samples were adhered using a carbon double-sided adhesive tape. The microstructure of samples was examined by means of transmission (TEM) and scanning transmission electron microscopy (STEM) using a 200 kV JEM-2100 instrument (JEOL). The materials for TEM were ground in methanol and then the prepared suspension was placed onto a carbon coated copper holey grid.

The compositions of obtained materials were investigated using Fourier-transform infrared spectroscopy (FTIR) with a Vertex 70 v vacuum spectrometer (Bruker) in a range of 400–4000 cm<sup>-1</sup> employing a partial internal reflection device, Raman spectroscopy using a DXR Raman microscope (Thermo Scientific) at the excitation wavelength of 532 nm, X-ray diffraction (XRD) analysis using a DRON-3 diffractometer (Burevestnik) operated with Co K $\alpha$  radiation, and EDX spectroscopy with a 80 mm<sup>2</sup> X-Max EDX detector (Oxford Instruments).

The Au and Pt contents in the metal/BN(O) nanohybrids were determined using inductively coupled plasma mass spectrometry (ICP-MS) with a XSeries 2 unit (Thermo Fisher Scientific). For this purpose, 15 mg of the material were preliminarily dissolved in a mixture of concentrated acids (1 ml HNO<sub>3</sub> + 3 ml HCl + 1 ml HF) and the suspension was kept in a microwave at 220 °C for 20 min. The produced solution was adjusted to 50 ml and diluted 50 times. The composition of nanohybrid surfaces with the lateral dimension of the analyzed area of 0.7 mm was elucidated by means of X-ray photoelectron spectroscopy (XPS) using a PHI5000 VersaProbeII spectrometer (ULVAC-PHI, Inc.).

After subtracting Shirley-type background CasaXPS software was applied for spectra fitting.

The adsorption of CO and CO<sub>2</sub> molecules was studied by diffuse reflection IR spectroscopy (DRIFT). IR spectra were recorded at room temperature on a NICOLET "Protege" 460 spectrometer equipped with a diffuse reflection prefix in a range of 6000–400 cm<sup>-1</sup> with a step of 4 cm<sup>-1</sup>. For a satisfactory signal-to-noise ratio, 500 spectra were accumulated. CaF<sub>2</sub> powder was used as a standard. Before measuring the spectra, the samples in the form of a fraction were heated to a temperature of 400 °C at a rate of 5 °C/min and held for 2 h to remove physically adsorbed water and gases. Adsorption of CO and CO<sub>2</sub> was carried out at room temperature and an equilibrium pressure of 10–14 mmHg. The intensity of bands in the spectra was expressed in Kubelka-Munch units [29,30]. Data collection and processing were carried out using the OMNIC program. The spectra of adsorbed gases were represented as the difference between those recorded after and before adsorption.

### 2.4. Theoretical modeling

All calculations were performed using VASP [31,32] in the framework of density functional theory (DFT) with Perdew, Burke, and Ernzerhof (PBE) [33] exchange-correlation functional. The projector-augmented wave (PAW) based pseudopotentials were used to expand the plane wave basis sets with a cutoff energy of 400 eV. The DFT-D3 corrections [34] were used to take into account Van der Waals interactions. A metal nanoparticle (55 atoms) was placed on a pristine *h*-BN monolayer, as well on a *h*-BN monolayer with N vacancy, B vacancy, and N vacancy filled with O atom using periodic boundary conditions. The sorption energies of oxygen and hydrogen atoms were calculated as  $dE = E(X_{ads}) - E(X) - E(ads)$ , where  $E(X_{ads})$  is the energy of a metal particle with an adsorbed molecule,  $E(X)$  is the chemical potential of a hydrogen or oxygen atom, calculated from H<sub>2</sub> or O<sub>2</sub> molecule,  $E(ads)$  is the energy of structure on which hydrogen and oxygen are adsorbed (metal NP on a support).

## 3. Results

### 3.1. Structural characterization

FTIR spectra of BNNPs (annealed in vacuum at 1500 °C for 2 h) and BNNPsOx (annealed in air at 1100 °C for 2 min) samples are shown in Fig. 1a. The spectra reveal two main features: broad bands in a range of 781–808 cm<sup>-1</sup>, corresponding to out-of-plane B-N-B bending (R mode), and 1358–1379 cm<sup>-1</sup>, corresponding to in-plane B-N stretching vibrations (LO mode) [35]. In high-purity crystalline BN, stretching of *h*-BN network in tangential directions can lead to the appearance of additional adsorption band (T) at 1530–1545 cm<sup>-1</sup>. In our case, T and LO peaks are broadened and overlapped. The FTIR spectrum of the BNNPs sample is free from oxygen and O-H-associated peaks, thereby indicating the effectiveness of high-temperature purification process. After annealing in air, the FTIR spectrum exhibits well resolved BN oxidation peaks and a broad maximum at 3250 cm<sup>-1</sup> (O-H peak). FTIR spectra of all metal-decorated samples (Fig. 1b) reveal the increased absorbance to the right of the main *h*-BN peaks due to the presence of B-O bonds formed during either *h*-BN high-temperature oxidation (metal/BNNPsOx) or hydrolysis during nanohybrid synthesis (metal/BNNPs).

Fig. 1c compares XRD patterns of BNNPs, BNNPsOx, metal/BNNPs, and metal/BNNPsOx materials. The XRD patterns recorded in a 2θ range of 20–100° are shown in Fig. S1. Characteristic peaks from the *h*-BN phase and metallic Au (ICDD card 00-001-1172; lattice parameter  $a = 4.0699 \text{ \AA}$ ) and Pt (ICDD card 00-001-1190; lattice parameter  $a = 3.9120 \text{ \AA}$ ) compounds are clearly visible. The position of the second observed XRD peak from the *h*-BN phase is the same for all samples (49.4° 2θ), whereas the position of the first peak is significantly different (29.9–31.7° 2θ). The position of the second maximum is exactly halfway between the (100) peak of the *h*-BN (ICDD card No. 85-1068,

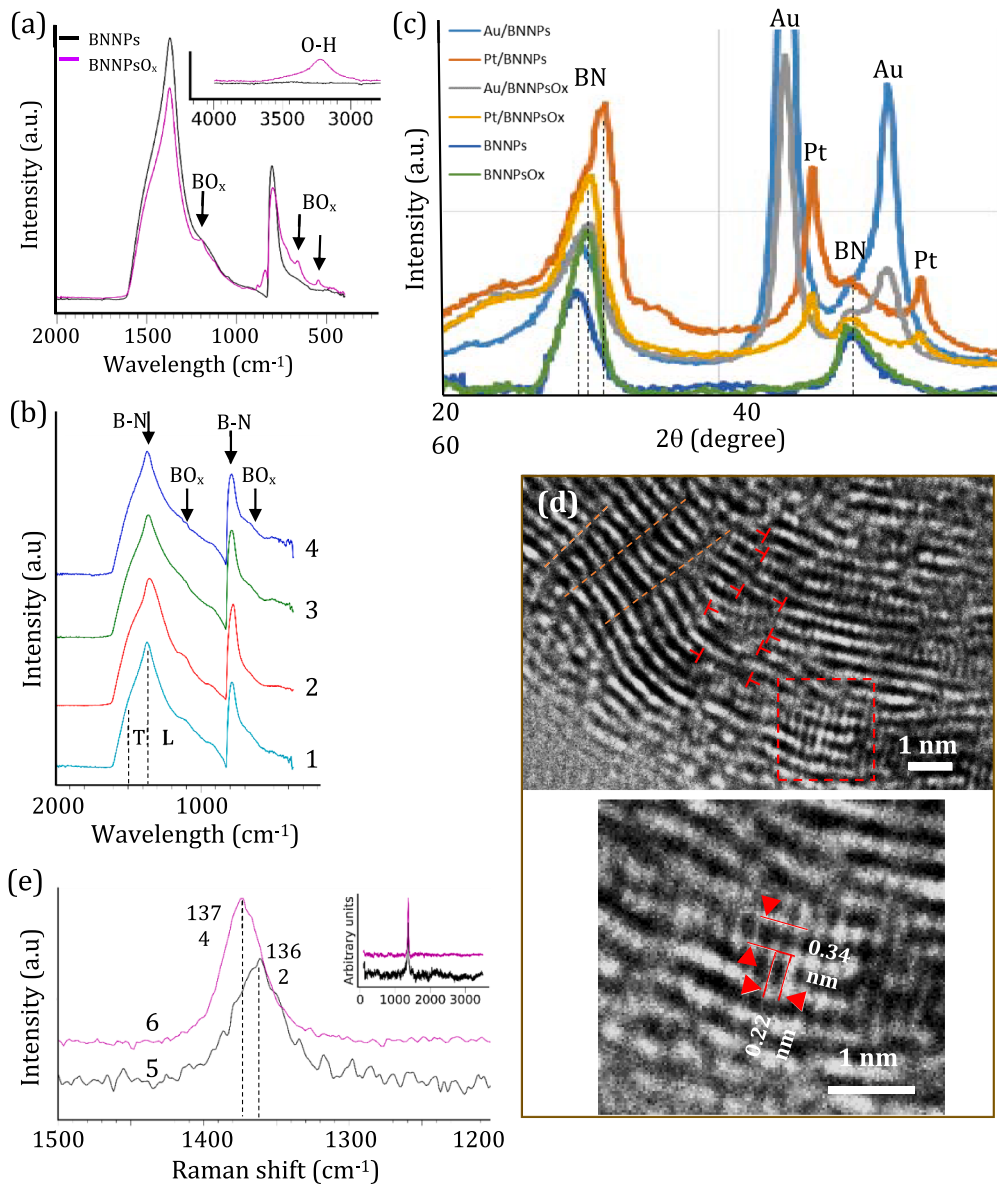


**Fig. 1.** FTIR spectra (a,b), XRD patterns (c) and Raman spectra (e). 1 – Au/BNNPs, 2 – Au/BNNPsOx, 3 – Pt/BNNPs, 4 – Pt/BNNPsOx. High-resolution TEM images (d) of turbostratic BN. Edge dislocations and interfaces are shown by symbol  $\perp$  and dashed lines, respectively.

$d=0.217$  nm) and the (101) peak of the rhombohedral BN (ICDD card 45–1171,  $d=0.212$  nm). This suggests the formation of turbostratic BN, *i.e.* highly defective BN consisting of hexagonal and rhombohedral BN nanocrystallites obeying specific orientation relationships [36].

This assumption is further confirmed by the results of TEM analysis. The high-resolution TEM images of turbostratic BN are depicted in Fig. 1d. The material is highly defective and contains numerous interfaces and edge dislocations. The size of individual BN nanocrystallite can be as small as 1.0–1.5 nm. Fig. 1d shows BN nanocrystallite in the hexagonal configuration.

The high-temperature vacuum-annealed BNNPs sample shows the symmetrical (001) BN XRD maximum, corresponding to an interplanar distance ( $d$ ) of 0.347 nm. After short-term annealing in air, the peak is down-shifted ( $d=0.338$  nm). Both Au decorated nanohybrids, as well as the sample with Pt NPs deposited on the oxidized support, exhibit (001) BN peaks at exactly the same position as their NP-free counterparts (29.9° (BNNPs) and 30.7° 20 (BNNPsOx)). All (001) BN peaks are wide with the full width at half-maximum (FWHM) values ranging from 8.5° to 14° 20, which, according to the Debye-Scherer equation, corresponds

to a crystallite size of  $\sim 1$  nm. Note that BNNPs are highly curved. The increased curvature of the graphitic planes can lead to FWHM broadening [37].

In the Pt/BNNPs, the (001) BN peak is asymmetrical and reveals two maxima located at 30.7 and 31.7 20 ( $d=0.328$  nm), suggesting different BN states. Overlapping of different domains of curved BN nanosheets can lead to broadening of XRD peaks. The  $\text{Au}_{(111)}/\text{BN}_{(001)}$  and  $\text{Pt}_{(111)}/\text{BN}_{(001)}$  intensity ratio decreases from 7.2 to 2.1 (Au) and from 0.7 to 0.3 (Pt) when comparing unoxidized and oxidized BN substrates.

The Raman spectra of synthesized supports display a clear band at  $1362\text{ cm}^{-1}$  for BNNPs, and  $1374\text{ cm}^{-1}$  for BNNPsOx, corresponding to  $E_{2g}$  mode of the *h*-BN phase (analogous to the G peak in graphene) (Fig. 1e). Crystalline *h*-BN displays an intrinsic  $E_{2g}$  vibration at  $1366\text{ cm}^{-1}$  [38] and the *h*-BN nanocrystals thinner than 5 layers exhibit blue-shift of  $4\text{ cm}^{-1}$  due to slightly shorter phonon modes [39]. Doping effect often shifts the G peak by  $\sim 10\text{ cm}^{-1}$  [40]. Raman scattering from turbostratic BN differs from that of crystalline BN; a full width at half-maximum (FWHM) of the Raman peak is significantly broader in the former material [41]. In our case, the FWHM values are  $37\text{ cm}^{-1}$

(BNNPs) and  $30\text{ cm}^{-1}$  (BNNPsOx) compared to  $\sim 9\text{ cm}^{-1}$  for a bulk BN. A red-shift of the  $E_{2g}$  peak seen for BNNPsOx in relation to BNNPs, is probably due to the oxygen intercalation and a weaker interaction between the basal planes in turbostratic BN.

**Fig. 2a,b,c** and **Fig. 2g,h,i** represent the characteristic XPS spectra of Au/BNNPs and Pt/BNNPs nanohybrids, respectively. All samples are mainly composed of B and N with minor amount of carbon and oxygen impurities. The curve fitting of XPS B1s signal of Au- and Pt-containing samples revealed similarity with respect to B environment. The XPS B1s spectra of Au/BNNPs (**Fig. 2a**) and Pt/BNNPs (**Fig. 2g**) samples can be fitted with a B-N component centered at BE= 190.6 eV and an additional contribution, namely B-N-O, centered at BE= 192.0 eV. The nitrogen peaks for all samples were fitted with a single N-B contribution centered at BE= 398.2 eV; this perfectly matches the BN environment.

The XPS analysis of Au/BNNPsOx (**Fig. 2d,e,f**) and Pt/BNNPsOx (**Fig. 2j,l**) nanohybrids did not reveal any significant differences in their elemental compositions.

Both Au4f and Pt 4 f signals can be fitted with a single component: Au (**Fig. 2c,f**) and Pt metals (**Fig. 2i,l**). Two specific features, namely: (i) the binding energy positions related to metallic peaks (Au 4 f 7/2 centered at BE= 84.2 eV (Au/BNNPs) and BE= 83.8 eV (Au/BNNPsOx) and Pt 4 f 7/2 centered at BE= 71.9 eV (Pt/BNNPs) and BE= 71.65 eV (Pt/BNNPsOx)); and (ii) the asymmetric shape of peaks, that is common for metals but not for their oxides, clearly indicate the metallic states [42]. Data on pristine *h*-BN powder measured under the same conditions were used as a reference.

SEM micrographs of the (Au,Pt)/BNNPs and (Au,Pt)/BNNPsOx nanohybrids are depicted in **Fig. 3**. Metal nanoparticles are uniformly

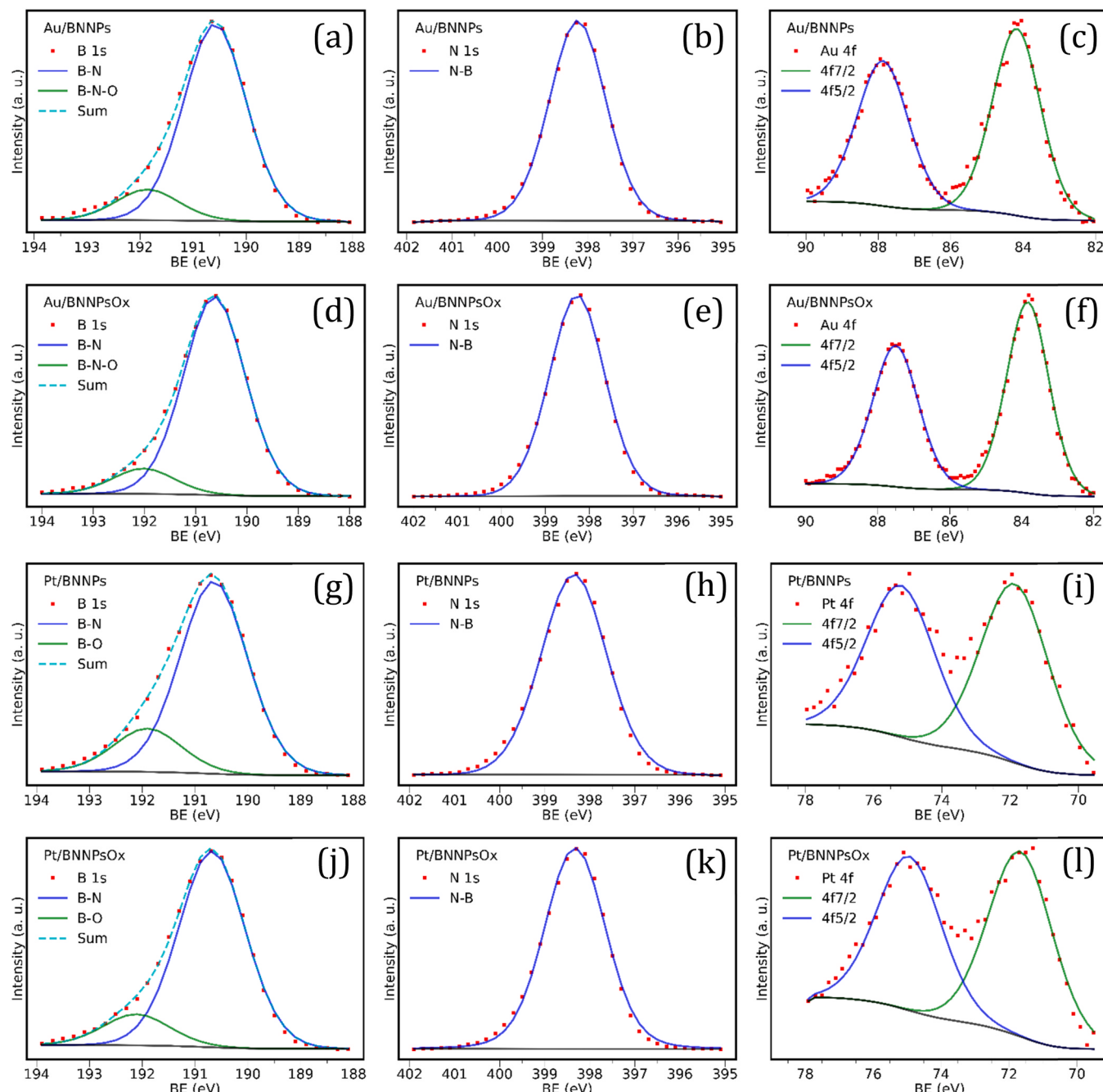


**Fig. 2.** XPS spectra of Au/BNNPs (a-c), Au/BNNPsOx (d-f), Pt/BNNPs (g-i) and Pt/BNNPsOx (j-l) nanohybrids and their curve fitting. B1s (a,d,g,j), N1s (b,e,h,k), Au4f (c,f) and Pt4f (i,l).

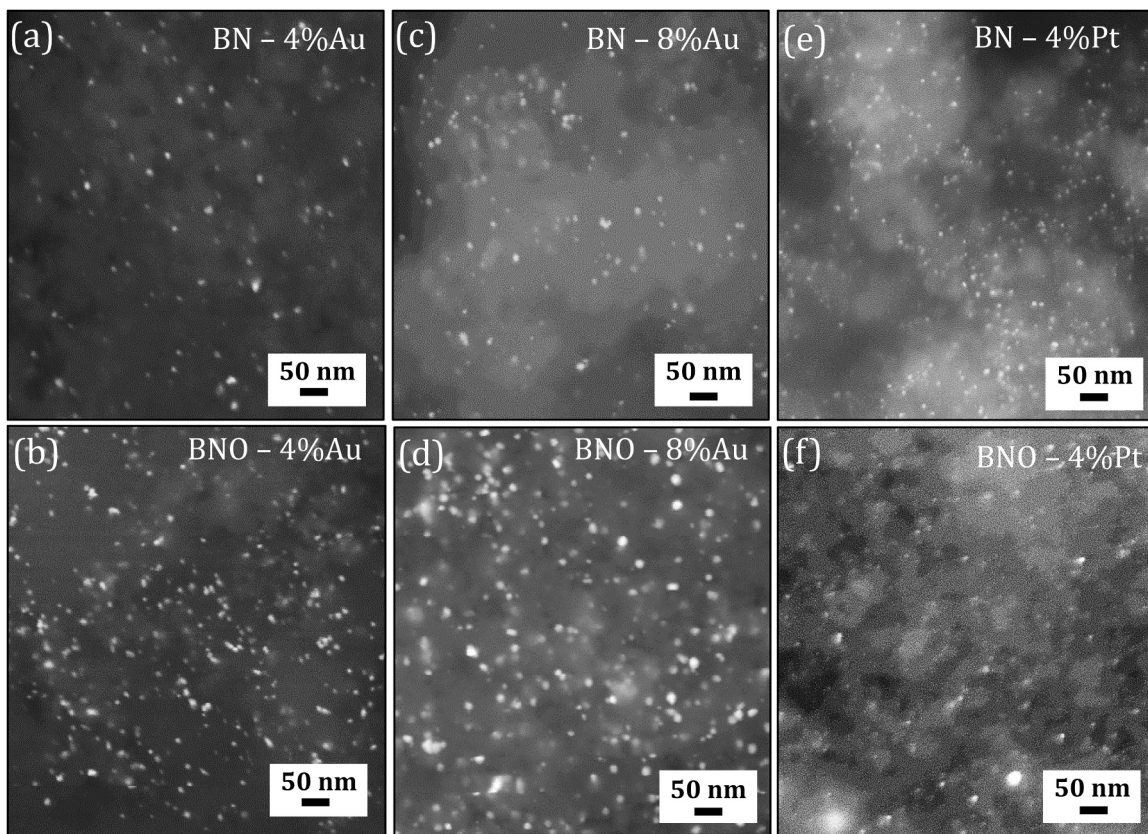


**Fig. 3.** SEM images of Au/BNNPs (a,c), Pt/BNNPs (e), Au/BNNPsOx (b,d), and Pt/BNNPsOx (f) nanohybrids.

distributed over the BN surfaces. Most of the particles are less than 10 nm in size.

TEM data manifests that *h*-BN nanoparticles have a sheet-like morphology and their lateral size varies from 20 to 50 nm (Figs. 4 and 5). Spherical metal nanoparticles have a dark contrast and densely populate the surface of *h*-BN nanosheets. On the oxidized BN surface, the size of Au nanoparticles is larger: 3–10 nm (4 wt% of Au) and 4–15 nm (8 wt% of Au) for BNNPs versus 6–20 nm (4 wt% of Au) and 5–20 nm (8 wt% of Au) for BNNPsOx. The size of Pt particles in the Pt/BNNPs and Pt/BNNPsOx nanohybrids changes within the range of 2–6 nm and 1–8 nm, respectively. Individual larger particles are observed in all types of nanohybrids. High-resolution TEM images of the Au and Pt nanoparticles are shown in Fig. 4. The observed interplanar distances are in a good agreement with Au (Fig. 4a,b) and Pt (Fig. 4c) phases. The interplanar distances of Au (ICDD card 00-001-1172) and Pt (ICDD card 00-001-1190) were used as references. Note that Au nanoparticle in Fig. 4a exhibits blurred border due to a slight defocus.

The contents of Au and Pt in the BNNPs- and BNNPsOx-based nanohybrids were determined by ICP-MS. According to the ICP-MS analysis, the metal contents in the Au/BNNPs samples were 4.4 and 8.1 wt%, depending on the metal loading dose. The Pt content in the Pt/BNNPs nanohybrids was 3.5 wt%. The BNNPsOx-based nanohybrids contained 2.6 and 6.7 wt% of Au (metal loading dose of 4 and 8 wt%, respectively) and 2.8 wt% of Pt. Thus, the content of noble metals in the BNNPsOx-based nanohybrids decreased compared with their oxygen-free counterparts.

Particle size distribution is presented in Fig. 6. It was obtained through statistical TEM image processing using 2–3 images for each nanohybrid and taking into account ~320–550 nanoparticles (depending on the composition). As seen in Fig. 6, the noble metal nanoparticle size distribution is different in the Au- and Pt-based systems. In the Au-based nanohybrids a broad particle size distribution is observed with the maxima at 6.7 (4 wt% of Au) and 8.9 nm (8 wt% of Au) for the Au/

BNNPs nanohybrids and 13.2–13.7 nm for the Au/BNNPsOx nanomaterials. In the case of high Au loading dose, the distribution is close to normal with a scatter of particle size from 3 to 18 nm in the Au/BNNPs (Fig. 6b) and from 3 to 31 nm in the Au/BNNPsOx (Fig. 6e). A decrease in the Au loading dose shifts the particle size distribution on the surface of BNNPs supports towards lower values, *i.e.* 2–14 nm (Fig. 6a). In contrast, the particle size distributions in the Pt/BN systems are either asymmetrical with a shift towards smaller nanoparticle size (Pt/BNNPs) or narrower with almost all particles being in a range of 1–6 nm (Pt/BNNPsOx).

### 3.2. Adsorption of CO and CO<sub>2</sub> molecules

During adsorption of carbon monoxide, no bands of characteristic valence vibrations with the C≡O bond were detected in the IR spectra. This indicates the absence of coordination unsaturated carrier cations (boron nitride) and deposited metals (Au and Pt) on the sample surface. Unlike monoxide, which interacts only with acidic centers (cations), carbon dioxide can interact with both acidic and basic centers (oxygen and OH groups) [29].

Fig. 7 shows the IR diffuse reflection spectra recorded on the samples after CO<sub>2</sub> adsorption and further desorption. It is seen that more CO<sub>2</sub> is adsorbed on the Au/BNNPsOx and Pt/BNNPsOx samples as compared to non-oxidized carriers. For Au-containing samples, the difference is about 2 times, and for samples decorated with Pt NPs, about 10 times. When comparing two catalysts with different type of metals, it can be seen that the Au/BNNPs and Au/BNNPsOx samples surpass Pt/BNNPs and Pt/BNNPsOx ones in their ability to adsorb carbon dioxide. All samples have weak CO<sub>2</sub> retention. Desorption in vacuum at room temperature leads to the disappearance of the adsorbed CO<sub>2</sub> bands from the spectra.

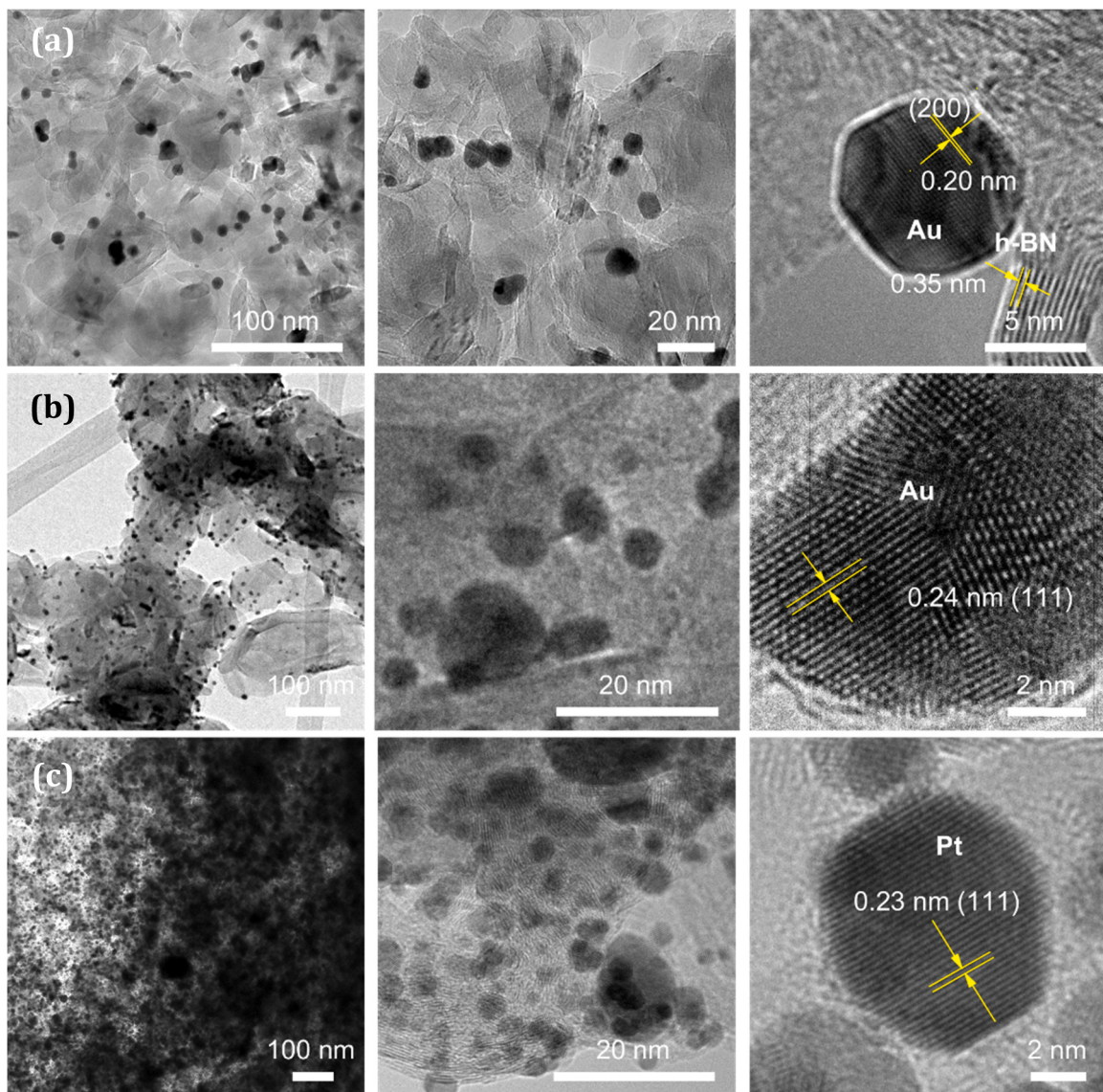


**Fig. 4.** TEM and HRTEM images of Au/BNNPs and Pt/BNNPs. (a) 4 wt% of Au, (b) 8 wt% of Au, (c) 4 wt% of Pt.

### 3.3. Catalytic activity of Au/BNNPs, Pt/BNNPs, Au/BNNPsOx and Pt/BNNPsOx in CO oxidation

Although after the report by Haruta in 1989 [7] researchers started to pay much attention to the ability of small Au nanoparticles to promote CO oxidation, Pt catalysts still remain among the most effective ones for this process [43]. Note, however, that although we used the same amount of catalyst for each catalytic reaction, the loading amount of Au and Pt was different. As reported above, surface oxidation state of BN support significantly affects the noble metal nanoparticle size distributions.

The results of catalytic activity tests in the CO oxidation reaction are presented in Fig. 8. The Pt/BN(O) nanohybrids exhibited significantly higher catalytic activity in CO conversion than the Au-based nanomaterials. The Pt catalyst activity starts already at a temperature less than 100 °C and full (100%) CO conversion is achieved at approximately 190 °C (Fig. 8c). Note that when using the Pt/BNNPsOx nanohybrid, the catalytic reaction starts and ends a bit earlier. The catalytic activity of Au/BN nanomaterials depends on the metal loading dose and the oxidized state of BN support. At a low Au loading dose of 4 wt% (Fig. 8a), the CO conversion starts at 155 °C and completes at 300 °C (Au/BNNPs) and 350 °C (Au/BNNPsOx). When the loading dose is 8 wt

% of Au (Fig. 8b), the activity of Au catalysts is only seen after reaching 200 °C and a complete CO conversion is observed at 280 °C (Au/BNNPsOx) and 400 °C (Au/BNNPs). The increase in catalytic activity when using BNNPsOx supports, as shown in Section 3.5., is apparently associated with an increase in the adsorption energy of oxygen molecules on the surface of metal NPs, which is more pronounced for Pt-based catalysts because of the strong interaction of Pt NP with the h-BN support.

### 3.4. Catalytic activity of Au/BNNPs, Pt/BNNPs, Au/BNNPsOx, and Pt/BNNPsOx in CO<sub>2</sub> hydrogenation

The results of catalytic activity tests in the reaction of CO<sub>2</sub> hydrogenation using the (Au,Pt)/BNNPs and (Au,Pt)/BNNPsOx nanohybrids pre-activated in hydrogen at 500 °C are presented in Table 1 and Fig. 8d. The main product of the CO<sub>2</sub> hydrogenation reaction is carbon monoxide. The formation of a small amount of methanol and light hydrocarbons, mainly methane, was also noticed, but the selectivity for these products did not exceed 5%. Pt-based catalysts are much more active in CO<sub>2</sub> hydrogenation than Au-based ones. This difference in the activity is explained by the different nature of these metals. The catalytic activity also depends on the oxidized state of support. The BNNPsOx-supported

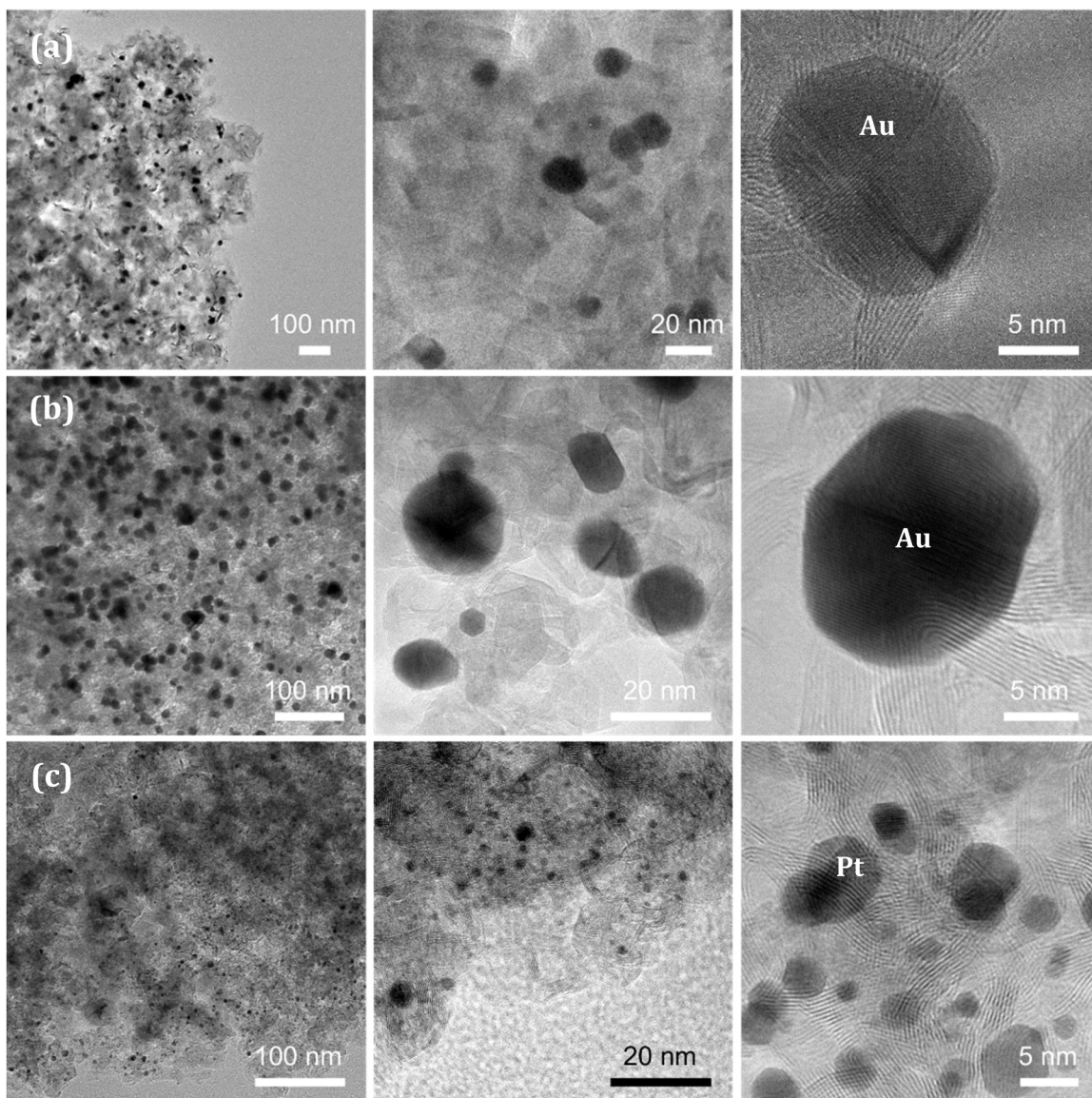


**Fig. 5.** TEM and HRTEM images of Au/BNNPsOx and Pt/BNNPsOx. (a) 4 wt% of Au, (b) 8 wt% of Au, (c) 4 wt% of Pt.

metal NPs catalysts show higher CO<sub>2</sub> hydrogenation activity than their unoxidized BNNPs-supported counterparts. It can be assumed that the presence of surface defects in the BNNPsOx improves the adsorption and activation of gas components on the catalyst surface under the reaction conditions. Fig. 9 shows the Arrhenius plot of CO formation rate. Samples with an oxidized substrate show a lower activation energies of 66 kJ/mol (Pt/BNNPsOx) and 61 kJ/mol (Au/BNNPsOx) compared to 86 kJ/mol (Pt/BNNPs) and 75 kJ/mol (Au/BNNPs). This may indicate a change in the contribution of one or another mechanism for the formation of carbon monoxide during the hydrogenation of CO<sub>2</sub>. For example, BNNPs and BNNPsOx carriers can either be directly involved in CO<sub>2</sub> hydrogenation reaction or indirectly, by changing the electronic state of the metal and through metal-support interaction. According to the results of catalytic studies, an increase in the activity of catalysts based on BNNPsOx in such different in nature reactions of CO<sub>2</sub> hydrogenation and CO oxidation can be associated with a change in the interaction of the catalyst surface with oxygen or oxygen-containing molecules of carbon oxides. Thus, the use of BNNPsOx as supports for active metal NPs most likely increases the number of adsorption sites of these molecules or their attachment strength.

The data on the hydrogenation of CO<sub>2</sub> on the (Au,Pt)/BNNPs and

(Au,Pt)/BNNPsOx systems are in good agreement with the data of IR spectroscopy of probe molecules. Table 1 shows a significant (up to 10 times) increase in the CO<sub>2</sub> conversion rate on the (Au,Pt)/BNNPsOx samples. In this case, the formation of CO increases significantly, which is obviously due to the better adsorption of CO<sub>2</sub> on oxidized BN. The formation of methanol and hydrocarbons changes insignificantly for oxidized and unoxidized BN, since, as well known, methanol is formed from CO during the hydrogenation of CO<sub>2</sub>, and CO is practically not retained in these systems.

### 3.5. Theoretical modeling

Comparison of the sorption energy of molecules on free-standing nanoparticles and nanoparticles on a BNNPs supports reveals the substrate influence on the sorption centers located on metal nanoparticles. For this purpose, four positions of the molecules above the metal particle in the direction from the substrate to the upper part of the nanoparticle were considered. In the DFT calculations, Au and Pt nanoparticles (NPs) were placed above the *h*-BN monolayer. Freestanding metal NPs were also considered. During oxidation, metal nanoparticles have the ability either to adsorb molecular oxygen with subsequent formation of

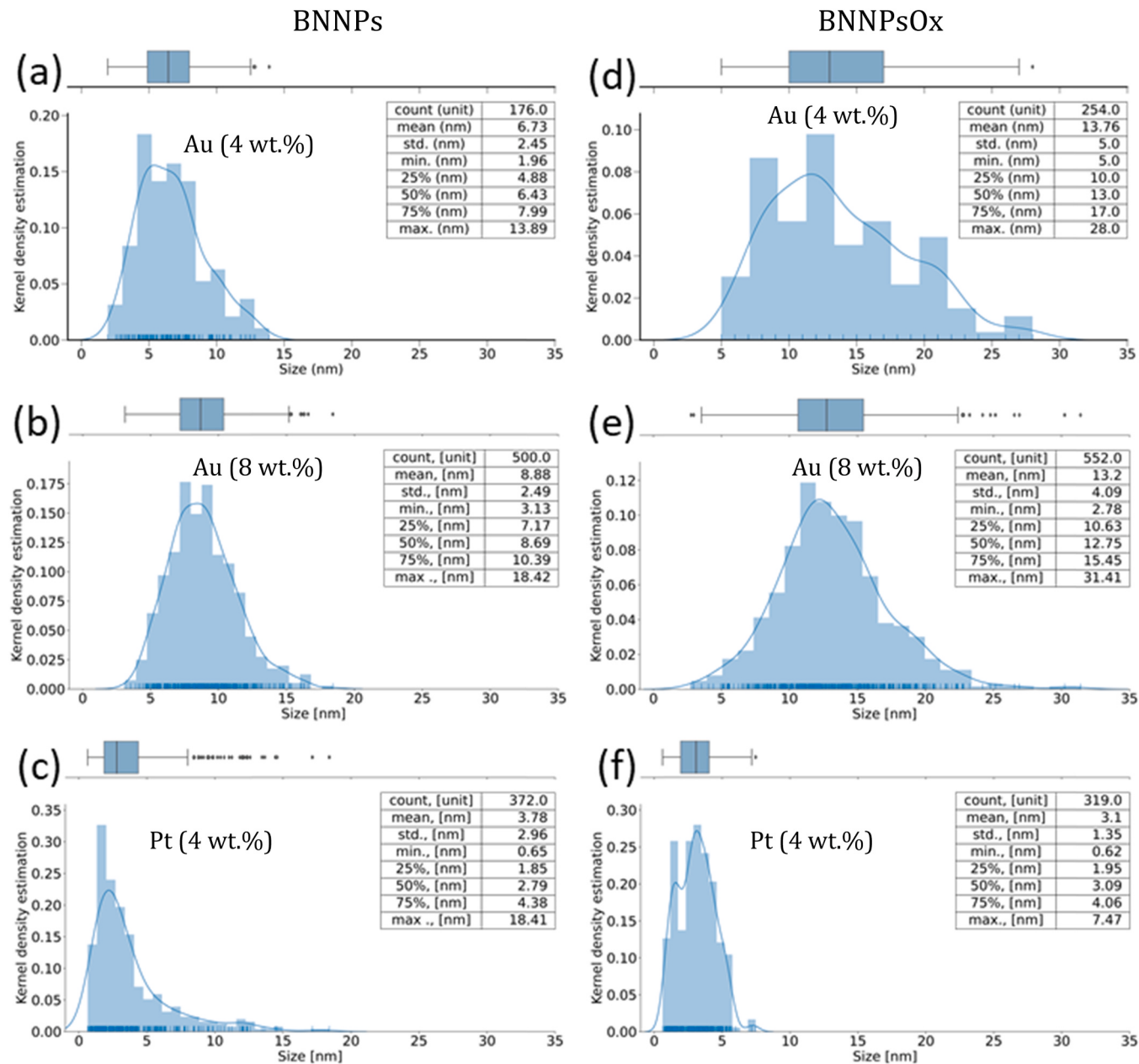


Fig. 6. Au (a,b,d,e) and Pt (c,f) particle size distribution in Au/BNNPs, Pt/BNNPs, Au/BNNPsOx, and Pt/BNNPsOx nanohybrids.

molecular complexes or dissociate an oxygen molecule.

The modeling results indicate that the oxidative behaviors of free-standing Au NP and Au/BNNP nanohybrid are similar (Fig. 10a,b). The oxygen sorption energy between these two systems differs by only  $\sim 0.1$  eV. This may indicate that in reactions involving hydrogen molecules the support consisting of pure defect-free *h*-BN would not have a significant effect. In reactions involving hydrogen, it is also equally important to study the sorption centers of metal nanoparticles and determine the difference in sorption energy relative to free-standing nanoparticles and nanoparticles on the support. The hydrogen sorption on the *h*-BN supported Au nanoparticle at the similar positions to freestanding Au NP (Fig. 10b) is not affected by the support at all, because the sorption energy difference between the two considered systems is below 0.05 eV. This indicates only a weak influence of the *h*-BN support onto Au nanoparticles.

In the case of Pt catalyst (Fig. 10c,d) the oxygen sorption energy at the Pt/BNNP interface is higher compared to freestanding Pt NP (the sorption energy difference varies in the range of 0.4–0.9 eV). This allows

one to conclude that the *h*-BN support affects the sorption properties of Pt NPs and thus leads to a change in the rate of reactions associated with oxygen sorption. On another side, based on the difference in the energy of hydrogen sorption on a pure Pt NP and a Pt NP on a support (Fig. 10d), the contribution of Pt/BNNPs interface to hydrogen sorption is relatively small (the difference from the freestanding Pt NP is 0.16 eV), but still higher than in the case of Au NP. Note that the hydrogen molecule tends to dissociate onto the Pt surface in all considered positions due to the low dissociation barrier of  $\sim 0.2$  eV [44]. In contrast, on the Au surface, hydrogen is primarily in the form of a physisorbed molecule.

The effect of the *h*-BN support on the Au and Pt NPs can be determined from the electron density distribution in the interface region. The difference in charge density distribution (CDD) was calculated as  $\rho = \rho(M/BN) - \rho(M) - \rho(BN)$ , where  $\rho(M/BN)$ ,  $\rho(M)$ , and  $\rho(BN)$  are CDD at the heterostructure interface, metal nanoparticle and *h*-BN sheet. The obtained CDD difference demonstrates a strong influence of the *h*-BN support onto charge redistribution at the Pt/*h*-BN interface (Fig. 11b). Thus, a strong interaction of the Pt NP with *h*-BN support can affect the

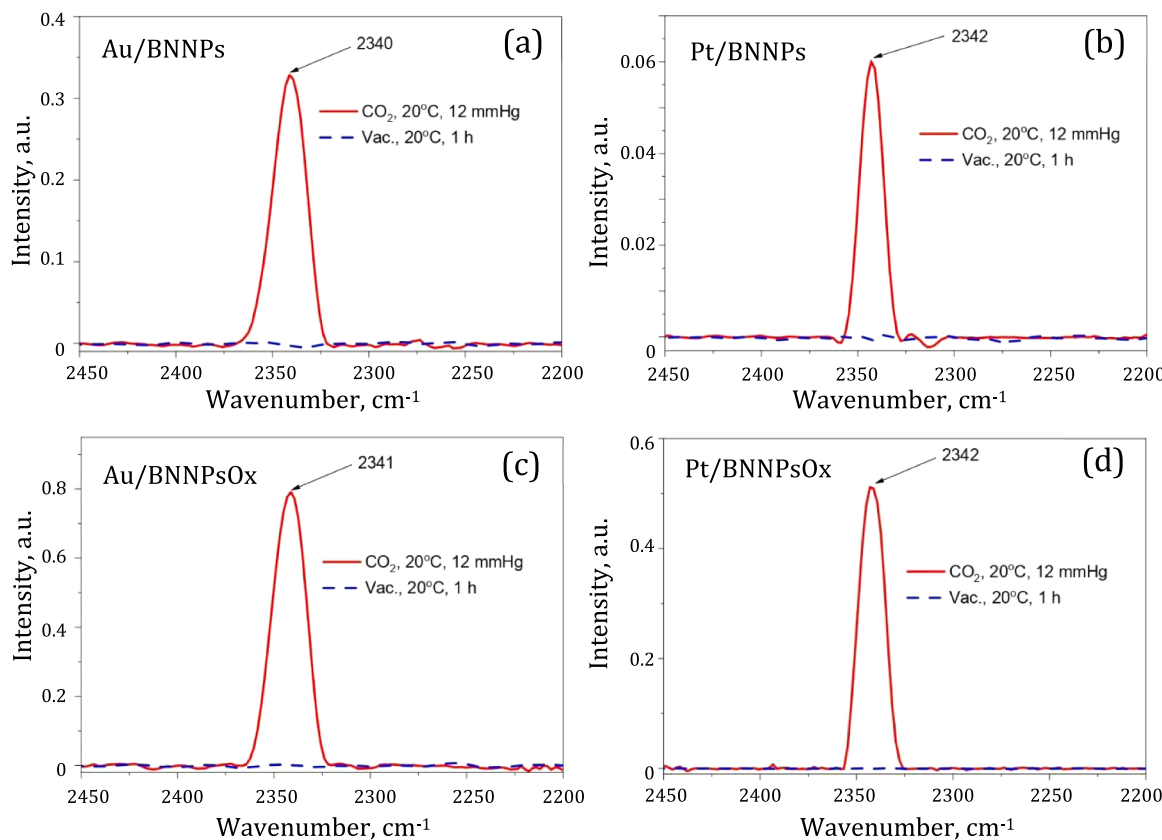


**Fig. 7.** Diffuse reflection spectra of Au/BNNPs (a), Pt/BNNPs (b), Au/BNNPsOx (c), and Pt/BNNPsOx (d) samples.

oxygen and hydrogen molecule absorptions by this noble metal. In contrast, no Au NP and *h*-BN interactions are observed (Fig. 11a). Here we consider metal nanoparticles and the charge distributed among all metal atoms. In the case of one single Au atom, the localization of charge on it can lead to its catalytic activity [45–47].

In the presence of B or N vacancies in *h*-BN, the substrate has an enhanced effect on the redistribution of electron density in metal particles (Fig. 11c–f). The influence of a vacancy is insignificant in the case of an Au nanoparticle. The redistribution of the electron density is only observed on two adjacent atomic layers near B and N vacancies (Fig. 11c,e). The interaction of a metal nanoparticle with a substrate is much stronger for the Pt/BN system, which also exceeds the interaction of a single metal atom interaction with an *h*-BN support [47,48]. In this case, the B vacancy has a stronger effect on the electron density distribution in the Pt nanoparticle in comparison with the N vacancy (Fig. 11d, f).

Finally, we calculated the redistribution of electron density in the case of substrate oxidation. Only the substitution of the nitrogen atom for the oxygen atom was considered (Fig. 11g, h), because it is energetically more favorable due to the lower formation energy [49]. It is seen that the presence of an oxygen impurity has no noticeable effect on the charge redistribution at the Au/BN(O) and Pt/BN(O) interfaces. Thus, the above-described difference in the distribution of the electron density between the systems remains in the case of substrate oxidation.

#### 4. Discussion

Our experimental and theoretical results indicate that *h*-BN supported Pt NP catalysts exhibit high catalytic activity in CO oxidation and CO<sub>2</sub> hydrogenation reactions. In addition, the oxidative state of BN support affects the catalytic activity. To understand the observed difference in the material catalytic behavior, several factors should be considered: (i) type of catalytically active centers and their adsorption

capacities, (ii) nanoparticle size and distribution over the support surface, (iii) oxidative state of metal NPs and support material, (iv) role of defects in *h*-BN, and (v) metal-support interactions (Fig. 12).

Au and Pt are typical members of noble metal and catalyst families. At the same time, the higher catalytic activities of Pt in the considered reactions of carbon monoxide oxidation and carbon dioxide hydrogenation are well known. The size of catalytically active metal NPs can play a significant role in the catalysis. This is clearly seen in the example of Au/BNNPs catalysts. When the average Au particle size decreases from 8.9 (8 wt% of Au) to 6.7 nm (4 wt% of Au), CO conversion starts and ends at temperatures of 45 °C and 100 °C lower, respectively (Fig. 7a,b). Note that with the same loading dose of 4 wt%, the noble metal nanoparticle size distribution is different in the Au- and Pt-based systems. In the Au-based catalysts (Fig. 6a,d), a broad particle size distribution is observed with a scatter of particle size from 2 to 14 nm (Au/BNNPs) and from 5 to 28 nm (Au/BNNPsOx). In contrast, the particle size distributions in the Pt/BN systems (Fig. 6c,f) are either asymmetrical with a shift towards smaller nanoparticles (Pt/BNNPs) or narrower with almost all particles being in a range of 1–6 nm (Pt/BNNPsOx).

Size and distribution of catalytically active particles on the support surface are the two main parameters affecting catalytic activity. Metallic Au is chemically inert; however, when it is in a form of small nanoparticles, typically below 10 nm, it becomes active for many chemical reactions [50]. This was clearly shown for some metal oxide supports [51]. In the case of Au/TiO<sub>2</sub> catalyst, an increase in the turnover frequency (TOF) is observed when the size of Au nanoparticles becomes less 5 nm [52]. The tendency is opposite for Pt/SiO<sub>2</sub> catalyst. Au NPs size effect affects the CO adsorption, which occurs at the metal surface defects (ledges, edges and corners), whereas the reaction with O<sub>2</sub> proceeds at the periphery of Au NPs. Even a slight increase in NP size can lead to a marked deterioration of catalytic performance in terms of offset and full conversion temperatures [20]. Thus, small size of Pt particles and their narrow size distribution may be one of the prime factors

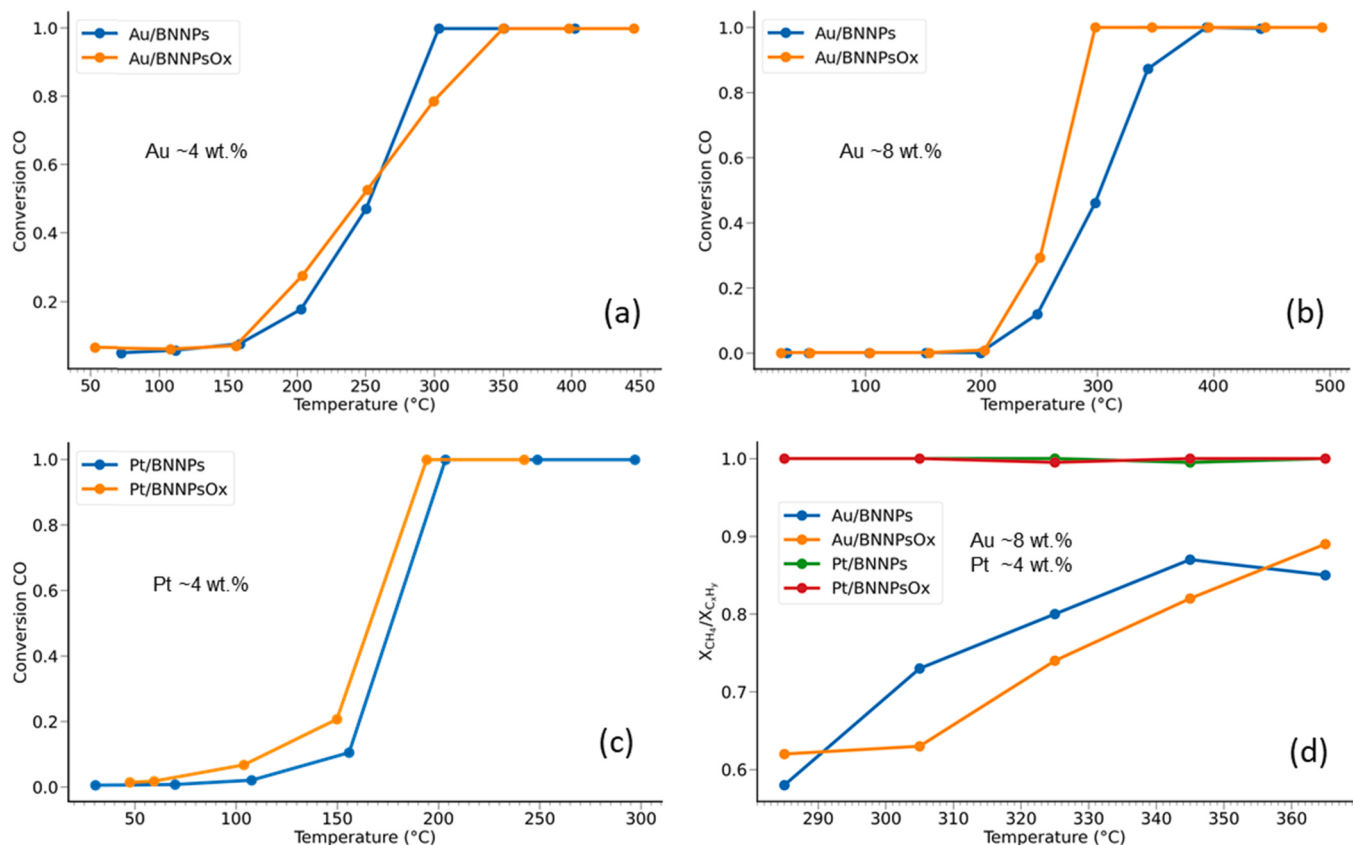


**Fig. 8.** Comparative catalytic activities of Au/BNNPs, Pt/BNNPs, Au/BNNPsOx, and Pt/BNNPsOx nanohybrids in the CO oxidation (a-c) and CO<sub>2</sub> hydrogenation (d) reactions; (d) proportion of methane among the hydrocarbon products of the CO<sub>2</sub> hydrogenation.

**Table 1**

The total rate of CO<sub>2</sub> hydrogenation and the rate of the main products formation as a function of temperature.

| Sample     | T, °C | Reaction rate of CO <sub>2</sub> hydrogenation, mol CO <sub>2</sub> × kg <sub>cat</sub> <sup>-1</sup> × h <sup>-1</sup> |  |   |       |
|------------|-------|---|--|---|-------|
|            |       | CO formation  | C <sub>x</sub> H <sub>y</sub> formation (×10 <sup>-2</sup> ) | CH <sub>3</sub> OH formation (×10 <sup>-2</sup> ) | Total |
| Au/BNNPs   | 285   | 0.2   | 0.3  | 0.0   | 0.2   |
|            | 305   | 0.4   | 0.4  | 1.7   | 0.4   |
|            | 325   | 0.6   | 0.8  | 2.2   | 0.6   |
|            | 345   | 1.0   | 1.4  | 2.7   | 1.0   |
|            | 365   | 1.6   | 2.0  | 3.9   | 1.6   |
| Pt/BNNPs   | 285   | 1.3   | 5.8  | 2.0   | 1.4   |
|            | 305   | 2.6   | 10.9   | 2.9   | 2.7   |
|            | 325   | 4.7   | 20.9   | 3.5   | 5.0   |
|            | 345   | 8.1   | 41.3   | 3.4   | 8.6   |
|            | 365   | 13.6  | 74.4   | 3.0   | 14.3  |
| Au/BNNPsOx | 285   | 0.7   | 0.3  | 0.0   | 0.7   |
|            | 305   | 1.2   | 0.6  | 2.3   | 1.3   |
|            | 325   | 1.8   | 0.7  | 3.3   | 1.8   |
|            | 345   | 2.7   | 1.0  | 4.7   | 2.7   |
|            | 365   | 3.7   | 1.6  | 4.9   | 3.7   |
| Pt/BNNPsOx | 285   | 3.5   | 6.4  | 1.9   | 3.5   |
|            | 305   | 5.5   | 10.9   | 3.6   | 5.6   |
|            | 325   | 8.7   | 18.8   | 4.4   | 9.0   |
|            | 345   | 13.4  | 30.6   | 6.2   | 13.7  |
|            | 365   | 20.6  | 45.7   | 7.0   | 21.1  |

explaining high catalytic activity of the Pt/BNNPs and Pt/BNNPsOx materials.

Not only the size, but also the distribution of the catalytically active NPs over the carrier surface is important. The Au/h-BN sample with an average Au NPs diameter of 6.7 nm, homogeneously distributed over the surface of h-BN nanoflakes, showed a higher catalytic activity in CO conversion than Au/BN material with Au NPs about 4 nm in size mainly located at the edge of h-BN (100% conversion *versus* 25% at 300 °C)

[53]. Fig. 5 shows that individual Pt NPs are covered with several atomic h-BN layers, and, therefore, some of the CO and O<sub>2</sub> molecules can penetrate to the metal through these overlayers. This intercalation process can promote catalytic reactions [54]. In contrast, encapsulation of Pt NPs by BO<sub>x</sub> overlayers can suppress the adsorption of CO and H<sub>2</sub> molecules on their surfaces and slow down the catalytic reaction [55]. However, it was speculated that partial removal of the oxide layer can create new Pt-BO<sub>x</sub> interfaces, which lead to enhanced catalytic activity

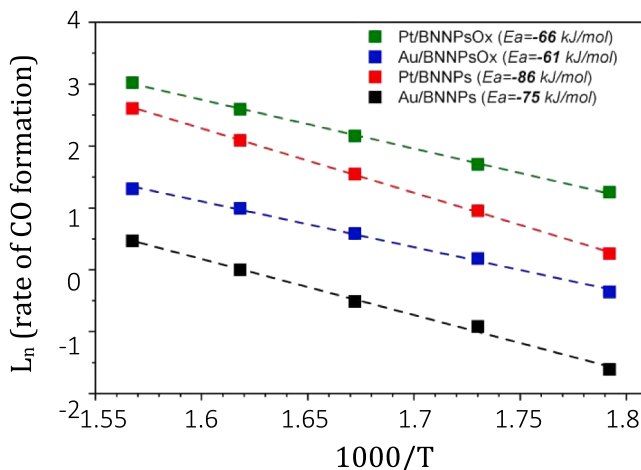


Fig. 9. Arrhenius plot of CO formation rate.

[56].

The results of DFT calculations indicate the stronger Pt/BNNPs interactions than for the Au/BNNPs counterparts. This might explain the lower temperature of CO oxidation in the Pt/BNNPs system. The BN support provides electrons to the Pt NPs, which assists the overall CO oxidation. At the same time, the noble metal/BNNPs interface does not seem to greatly affect the hydrogen sorption, because the dissociation barrier for hydrogen molecule is rather low.

h-BN nanostructures often contain various defects, such as vacancies, interstitial atoms, dislocations, grain boundaries, and edges; some of them can be seen in Fig. 1c. Atomic defects in the mechanically exfoliated monolayer h-BN were observed by STEM technique [57]. These defects on the surface of catalyst support can significantly contribute to the interaction with the adsorbate molecule [58,59]. In the present study, we have utilized h-BN substrates after various pre-treatment procedures: vacuum purification at 1500 °C and annealing in air at 1100 °C, which are believed to result in different defect structures. It is known that even upon mild oxidation of h-BN in O<sub>2</sub> or NO<sub>2</sub> at temperatures of 400–450 °C, a thin boron oxide (BO<sub>x</sub>) overlayer is formed [60]. During further treatment in aqueous solutions, a part of boron oxide can

be removed and B-vacancies can form.

It is worth noting that, according to numerous theoretical studies, even defect-free h-BN cannot be considered as an inert support for Au atoms [14,61,62]. Weak interaction of Au atoms with the h-BN support leads to an increase in the adsorption and activation of the adsorbed O<sub>2</sub> by the electron-pushing mechanism. Although the defect-free h-BN surface is not a good electron donor for the Au-O<sub>2</sub> bond, it promotes an electron transfer from the deposited Au to the adsorbed O<sub>2</sub>. During Au atom interactions with N and B defects located at the Au-BN interface, the charge transfer occurs to Au atoms in the case of N vacancies and in the opposite direction in the case of B vacancies. An excess of positive or negative charge on an Au atom can significantly affect its catalytic properties. This may explain a downshift in the temperature of full CO conversion by 100 °C observed in the Au/BNNPsOx sample as compared to Au/BNNPs counterpart with 8 wt% of Au, despite the significantly larger Au particle size (13 *versus* 9 nm). For the sake of completeness, note that moisture can also play an important role in the CO oxidation, especially in the case of Au/BN catalysts, due to activation of molecularly adsorbed O<sub>2</sub> and CO [53,63].

The contribution of various factors (particle size, chemical state, and defectiveness of the substrate surface) can be seen in the example of catalysts based on Au (Fig. 8a,b). When comparing Au/BNNPs nanohybrids, it can be concluded that in materials with 4 wt% Au, CO conversion starts 45 °C and ends 100 °C earlier due to the particle size effect (6.7 nm *versus* 9 nm). In the Au/BNNPs and Au/BNNPsOx nanomaterials with 4 wt% Au, the average metal particle size and their distribution differ significantly (6.7 nm (2–14 nm) and 14 nm (5–28 nm)), but both materials perform similarly up to 50% CO conversion. This suggests that the chemical state of a substrate surface and/or its defect structure also plays an important role. Surface defects are additional catalytic centers affecting CO<sub>2</sub> hydrogenation under the formation of CO through the carbonate mechanism [64,65]. Results of studying the influence of H<sub>2</sub>O on CO oxidation further support this hypothesis [53].

In Pt catalysts, at low temperatures, CO does not bind to metal atoms (there is no CO poisoning effect), which makes it easy to adsorb the O<sub>2</sub> molecule and form CO<sub>2</sub>. The interaction of Pt with BN defects at the metal-support interface promotes the O<sub>2</sub> adsorption and regulates the CO oxidation, which probably occurs *via* the Eley-Rideal mechanism [66]. BN surface acts as a Lewis acid to accept electrons from metal when Pt sits on B-vacancies, and, in the case of Pt on N-vacancies, serves

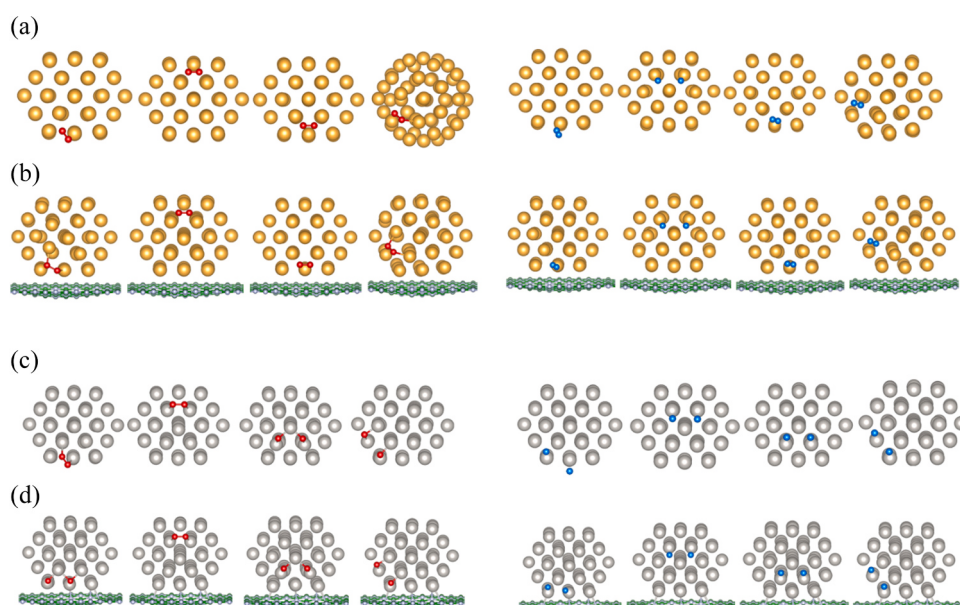
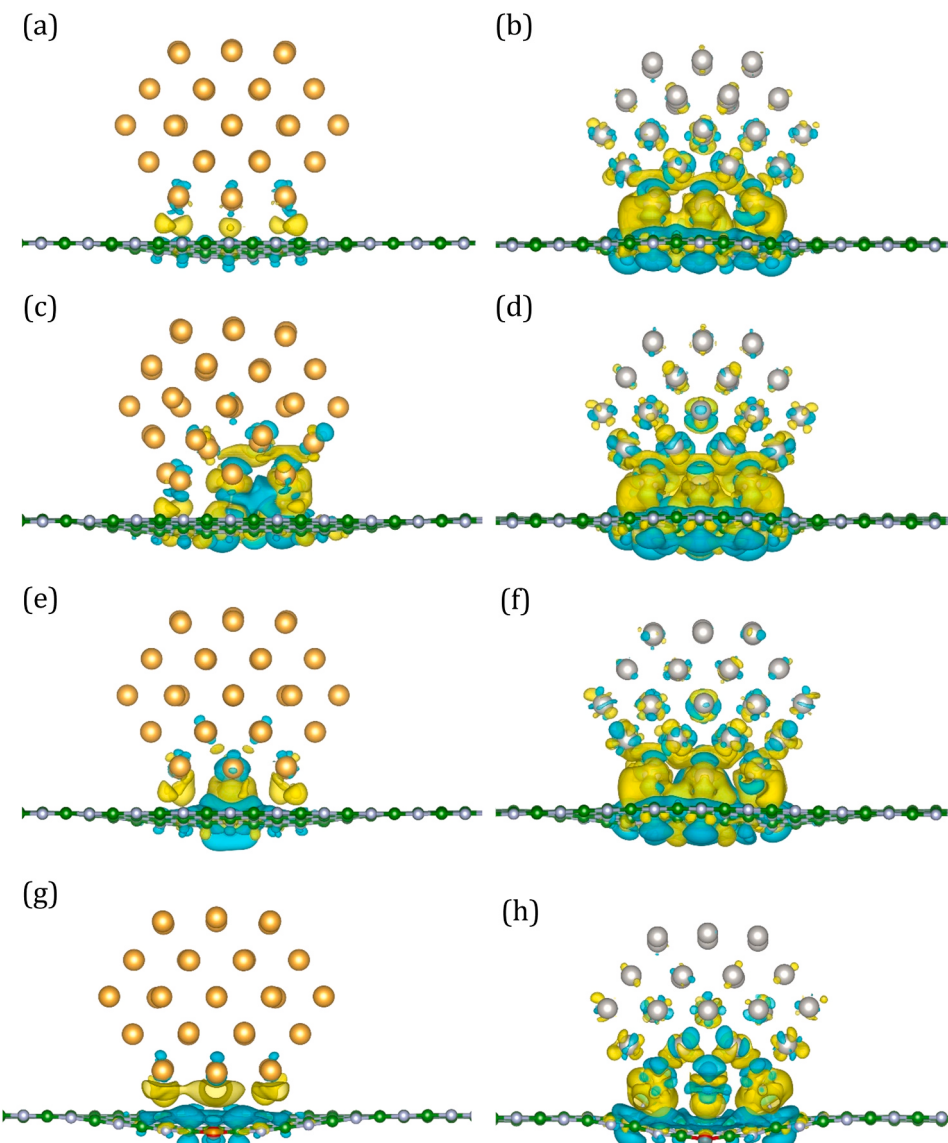


Fig. 10. Oxygen and hydrogen molecules at different positions on: (a) freestanding Au NP, (b) Au NP on h-BN, (c) freestanding Pt NP, (d) Pt NP on h-BN. The Au, Pt, B, N, O and H are marked by yellow, large gray, green, small gray, red and blue spheres, respectively.



**Fig. 11.** Spatial charge difference distribution of Au and Pt NPs on *h*-BN: pristine *h*-BN (a,b), *h*-BN with (c,d) B vacancy, (e,f) N vacancy, and N vacancy filled with oxygen atom (g,h). The iso-value is  $0.001e/\text{\AA}^3$ . Positive and negative iso-surface value corresponds to yellow and cyan colors. The Au, Pt, B, N, and O atoms are marked by large yellow, large gray, green, small gray, and red spheres, respectively.

as a Lewis base for donating electrons to Pt [67]. The catalytic cycle consists of  $\text{O}_2$  adsorption,  $\text{O}_2\text{-CO}$  interaction near the metal-support interface with the formation of a peroxide-like complex and its dissociation with the formation of  $\text{CO}_2$  molecule. Subsequently, the active center is regenerated by the interaction of the adsorbed O atom and the CO molecule in the gas phase (Fig. 12). Although Pt nanoparticles on the surface of pre-oxidized BN support show a slightly higher catalytic activity compared with the Pt/BNNPs nanohybrids, the difference is not so significant.

When comparing the CO oxidation kinetics of Au/BNNPs and Au/BNNPsOx nanomaterials, it can be seen that reaction starts at the same temperature of  $200^\circ\text{C}$ , but then the kinetic curves begin to diverge. As a result, the CO conversion on the oxidized substrate ends  $100^\circ\text{C}$  earlier (Fig. 8b). The results of DFT analysis show that defects in the *h*-BN crystal lattice facilitate the interaction of the carrier with the metal nanoparticle. As a result of a change in the electronic state of metal, the adsorption and activation of the oxygen molecule are enhanced. Thus, a CO molecule in the gas phase has a better chance of interacting with oxygen to form  $\text{CO}_2$ .

During the hydrogenation of  $\text{CO}_2$  the formation of methanol and

light hydrocarbons often occurs through the CO generation stage (reverse water-gas shift reaction – r-WGSR) [68–70], which is usually faster compared to the methanol and light hydrocarbon formation stages. In the latter case, low catalyst activity can be associated with a high  $\text{CO}_2$  volumetric flow rate and, consequently, short contact time of the reagents with the catalyst [71,72]. Usually, the hydrogenation of  $\text{CO}_2$  is accompanied by the following reactions:



The measured rates of these reactions are shown in Table 1. It can be seen that Pt-based catalysts exhibit significantly higher activity compared with the Au-based nanomaterials and the overall rate of  $\text{CO}_2$  hydrogenation is mainly determined by CO formation (Fig. 12). Note that the catalytic activity of Pt/BN samples was similar to that reported for Ru catalysts on a porous BN support [73].

Both Au/BNNPsOx and Pt/BNNPsOx catalysts demonstrated higher

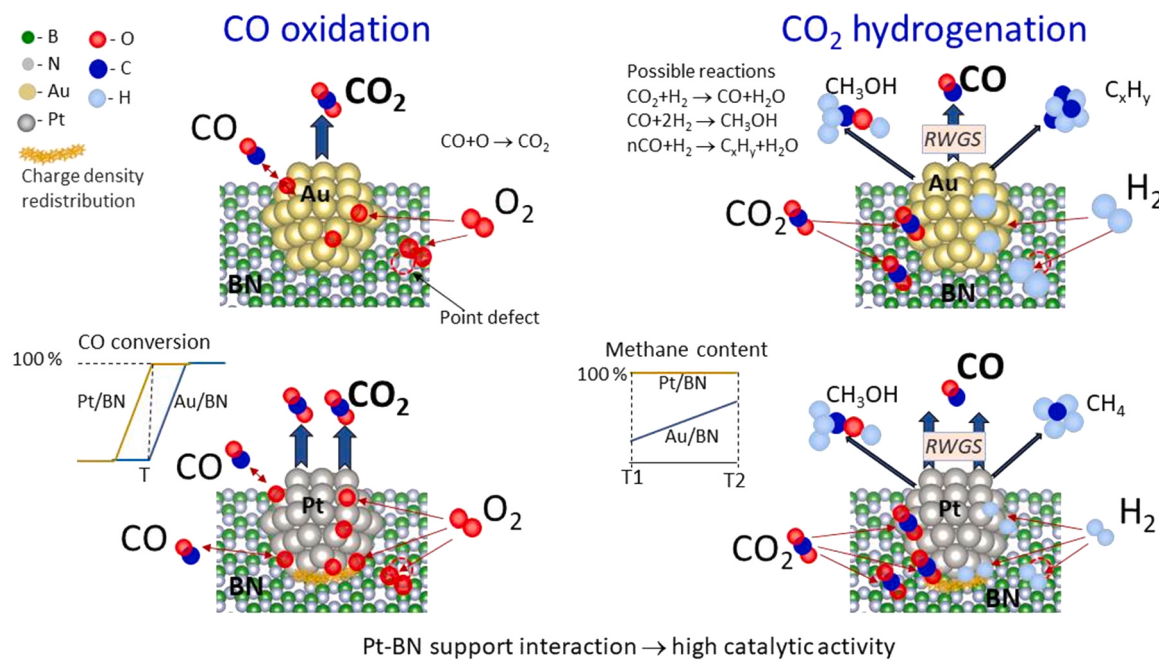


Fig. 12. Schematics of possible catalytic reaction pathways.

catalytic activity in CO<sub>2</sub> hydrogenation than these noble metals on the BNNPs supports. Since the main reaction product for all studied samples was CO with a selectivity of more than 95%, it makes sense to consider the reaction mechanism. Three main WGS reaction mechanisms on heterogeneous catalysts have been proposed: namely, formate, carbonyl, and carbonate [74,75]. The formate mechanism implies the presence of active centers on the surface of oxidized supports, where the activation of the CO<sub>2</sub> molecule occurs, followed by its transformation into CO through the formation of a formate complex. The carbonyl mechanism can be considered as a redox reaction, *i.e.* it assumes the adsorption of CO<sub>2</sub> molecule on the metal surface with the oxidation of metal, the formation of a carbonyl complex, the reorganization of this complex, and the CO formation. Subsequently, catalytically active metal is regenerated by hydrogen. In the case of carbonate mechanism, CO is formed at the defects located at the metal-support interface [75]. It is assumed that the adsorption of a CO<sub>2</sub> molecule occurs simultaneously both at the support and deposited metal, followed by the formation of a carbonate complex, its restructuring, and CO molecule release.

In conclusion, we note that a direct comparison of the Au- and Pt-based catalytic systems is difficult even at the same metal loading, since the materials differ in size and distribution of nanoparticles, which are also affected by the oxidation state of a support. For each specific system, various factors, such as nanoparticle dispersion, oxidized and defective state of the support, and metal-support interactions must be considered in synergy. For the CO oxidation and CO<sub>2</sub> hydrogenation reactions, the adsorption of CO and O<sub>2</sub>, and H<sub>2</sub> species on the surfaces of metal nanoparticles and h-BN support should be taken into account. The Pt-based hybrid nanomaterials synthesized herein showed high catalytic activity in the reactions of CO oxidation and CO<sub>2</sub> hydrogenation, their characteristics are not inferior to the Pt/TiO<sub>2</sub> catalysts described elsewhere [76] and superior in activity to most Cu-based catalysts that are often used during the regarded processes [68].

## 5. Conclusions

Au/h-BN(O) and Pt/h-BN(O) nanohybrids have been fabricated using an impregnation method on plasma-chemical synthesized h-BN supports and analyzed as promising catalysts in carbon monoxide oxidation and carbon dioxide hydrogenation reactions. The important

findings are:

- 1) At the same metal loading dose of 4 wt%, nanoparticle dispersion in the Pt- and Au-based catalysts is different. In the Au-based materials, a broad particle size distribution is observed; the particle size is 2–14 nm (Au/h-BN) and 5–28 nm (Au/h-BNO), with the maxima at 6.7 nm and 14 nm, respectively. In the Pt/h-BN(O) systems most of the Pt particles are below 6 nm in size peaked at 3 nm (h-BNO) and 4 nm (h-BN).
- 2) The Pt/h-BN(O) nanohybrids have shown a high catalytic activity in CO conversion. The Pt/h-BN catalytic activity starts at a temperature below 100 °C and full (100%) CO conversion has been achieved at ~190 °C. When using the Pt/h-BNO nanohybrids, the catalytic reaction starts and finishes at slightly lower temperatures. The activity of Au catalysts at the same loading dose as Pt is only noticed after reaching 150 °C and complete CO conversion has been observed at 300 °C (Au/h-BN) and 350 °C (Au/h-BNO).
- 3) The Pt-based catalysts also show a high activity in carbon dioxide hydrogenation reaction. The main product of the CO<sub>2</sub> hydrogenation reaction is carbon monoxide. In the case of Pt/h-BN catalysts, methane is the only hydrocarbon by-product of the CO<sub>2</sub> hydrogenation. The significantly higher CO<sub>2</sub> conversion rate observed on the BNNPsOx-supported Au and Pt catalysts is associated with better CO<sub>2</sub> adsorption on oxidized BN.
- 4) The results of DFT calculations indicate that the h-BN support increases the oxygen sorption properties at the Pt/h-BN interface and therefore affects the rate of oxygen-associated reactions. In addition, h-BN support leads to a charge density distribution at the Pt/h-BN interface. The strong Pt-h-BN interactions can affect oxygen and hydrogen molecule absorptions, thereby accelerating chemical reactions.
- 5) The results indicate that the Pt/h-BN(O) nanohybrids are an efficient and universal catalyst in carbon monoxide oxidation and carbon dioxide hydrogenation reactions. The BNO-based catalysts show slightly higher activity compared to their oxygen-free counterparts.

## CRediT authorship contribution statement

Andrey M. Kovalskii: Conceptualization, Methodology,

Investigation, Formal analysis. **Ilia N. Volkov:** Conceptualization, Investigation, Visualization. **Nikolay D. Evdokimenko:** Investigation, Visualization. **Olga P. Tkachenko:** Investigation, Visualization. **Denis V. Leybo:** Investigation, Visualization. **Ilya V. Chepkasov:** Methodology, Validation. **Zakhar I. Popov:** Methodology, Validation. **Andrei T. Matveev:** Investigation, Visualization. **Anton Manakhov:** Data curation, Formal analysis. **Elizaveta S. Permyakova:** Investigation, Visualization. **Anton S. Konopatsky:** Investigation, Validation, Project administration. **Alexander L. Kustov:** Investigation, Validation, Formal analysis. **Dmitri V. Golberg:** Formal analysis, Writing – review & editing. **Dmitry V. Shtansky:** Supervision, Writing – review & editing.

### Declaration of Competing Interest

The authors declare that they have no known competing financial interests or personal relationships that could have appeared to influence the work reported in this paper.

### Acknowledgements

The authors gratefully acknowledge the financial support from the Russian Science Foundation (Agreement No. 20-79-10286) in the part of catalyst fabrication, characterization, and testing in CO<sub>2</sub> hydrogenation reaction and the Ministry of Education and Science of the Russian Federation (Increase Competitiveness Program of NUST "MISIS" No. K2-2020-009) in the part of theoretical calculations. I.N.V. thanks the Russian Foundation for Basic Research (Agreement No. № 20-33-90070 \20) in the part of CO oxidation tests. D.G. is grateful to the Australian Research Council (ARC) for granting a Laureate Fellowship FL160100089 (result discussion and editing). Z.I.P. is grateful to the Joint Supercomputer Center of the Russian Academy of Sciences, the Information Technology Centre of Novosibirsk State University, and the Materials Modelling and Development Laboratory at NUST "MISIS" (supported via the grant from the Ministry of Education and Science of the Russian Federation No. 14. Y26.31.0005) for providing access to the cluster computational resources.

### Appendix A. Supporting information

Supplementary data associated with this article can be found in the online version at [doi:10.1016/j.apcatb.2021.120891](https://doi.org/10.1016/j.apcatb.2021.120891).

### References

- [1] P. Gélin, M. Primet, Complete oxidation of methane at low temperature over noble metal based catalysts: a review, *Appl. Catal. B Environ.* 39 (2002) 1–37, [https://doi.org/10.1016/S0926-3373\(02\)00076-0](https://doi.org/10.1016/S0926-3373(02)00076-0).
- [2] M. Schmal, Heterogeneous catalysis and its industrial applications, Springer (2016), <https://doi.org/10.1007/978-3-319-09250-8>.
- [3] A.S. Ivanova, E.M. Slavinskaya, R.V. Gulyaev, V.I. Zaikovskii, OA Stonkus, I. G. Danilova, L.M. Plyasova, I.A. Polukhina, A.I. Boronin, Metal-support interactions in Pt/Al<sub>2</sub>O<sub>3</sub> and Pd/Al<sub>2</sub>O<sub>3</sub> catalysts for CO oxidation, *Appl. Catal. B Environ.* 97 (2010) 57–71, <https://doi.org/10.1016/j.apcatb.2010.03.024>.
- [4] S. Monyanon, A. Luengnaruemitchai, S. Pongstabodee, Preferential oxidation of carbon monoxide in simulated reformed gas over PtAu/Ce<sub>x</sub>Zn<sub>y</sub>O<sub>2</sub> catalysts, *Int. J. Hydrog. Energy* 35 (2010) 3234–3242, <https://doi.org/10.1016/j.ijhydene.2010.01.070>.
- [5] D. Cameron, R. Holliday, D. Thompson, Gold's future role in fuel cell systems, *J. Power Sources* 118 (2003) 298–303, [https://doi.org/10.1016/S0378-7753\(03\)00074-0](https://doi.org/10.1016/S0378-7753(03)00074-0).
- [6] D. Pakhare, J. Spivey, A review of dry (CO<sub>2</sub>) reforming of methane over noble metal catalysts, *Chem. Soc. Rev.* 43 (2014) 7813–7837, <https://doi.org/10.1039/C3CS60395D>.
- [7] M. Haruta, N. Yamada, T. Kobayashi, S. Iijima, Gold catalysts prepared by coprecipitation for low-temperature oxidation of hydrogen and of carbon monoxide, *J. Catal.* 115 (1989) 301–309, [https://doi.org/10.1016/0021-9517\(89\)90034-1](https://doi.org/10.1016/0021-9517(89)90034-1).
- [8] J.L. Santos, P. Mäki-Arvela, A. Monzón, D.Y. Murzin, M.Á. Centeno, Metal catalysts supported on biochars: Part I synthesis and characterization, *Appl. Catal. B Environ.* 268 (2020), 118423, <https://doi.org/10.1016/j.apcatb.2019.118423>.
- [9] A. Mirescu, U. Prüße, A new environmental friendly method for the preparation of sugar acids via catalytic oxidation on gold catalysts, *Appl. Catal. B Environ.* 70 (2007) 644–652, <https://doi.org/10.1016/j.apcatb.2006.01.017>.
- [10] J. Huang, M. Haruta, Heterogeneous catalysis by gold clusters, Bridg. Heterog. Homog. Catal., John Wiley Sons, Ltd (2014) 397–424, <https://doi.org/10.1002/9783527675906.ch11>.
- [11] N. Iwasa, N. Takezawa, New supported Pd and Pt alloy catalysts for steam reforming and dehydrogenation of methanol, *Top. Catal.* 22 (2003) 215–224, <https://doi.org/10.1023/A:1023571819211>.
- [12] X. Wu, J. Yang, J.G. Hou, Q. Zhu, Defects-enhanced dissociation of H<sub>2</sub> on boron nitride nanotubes, *J. Chem. Phys.* 124 (2006), 054706, <https://doi.org/10.1063/1.2162897>.
- [13] Y.-H. Zhang, K.-G. Zhou, X.-C. Gou, K.-F. Xie, H.-L. Zhang, Y. Peng, Effects of dopant and defect on the adsorption of carbon monoxide on graphitic boron nitride sheet: A first-principles study, *Chem. Phys. Lett.* 484 (2010) 266–270, <https://doi.org/10.1016/j.cplett.2009.11.051>.
- [14] M. Gao, A. Lyalin, T. Taketsugu, CO oxidation on h-BN supported Au atom, *J. Chem. Phys.* 138 (2013), 034701, <https://doi.org/10.1063/1.4774216>.
- [15] A. Lyalin, A. Nakayama, K. Uosaki, T. Taketsugu, Theoretical predictions for hexagonal BN based nanomaterials as electrocatalysts for the oxygen reduction reaction, *Phys. Chem. Chem. Phys.* 15 (2013) 2809–2820, <https://doi.org/10.1039/C2CP42907A>.
- [16] X. Liu, T. Duan, Y. Sui, C. Meng, Y. Han, Copper atoms embedded in hexagonal boron nitride as potential catalysts for CO oxidation: a first-principles investigation, *RSC Adv.* 4 (2014) 38750–38760, <https://doi.org/10.1039/C4RA06436D>.
- [17] A. Trovarelli, J. Llorca, Ceria catalysts at nanoscale: how do crystal shapes shape catalysis? *ACS Catal.* 7 (2017) 4716–4735, <https://doi.org/10.1021/acscatal.7b01246>.
- [18] H. Mistry, A.S. Varela, S. Kühl, P. Strasser, B.R. Cuenya, Nanostructured electrocatalysts with tunable activity and selectivity, *Nat. Rev. Mater.* 1 (2016) 1–14, <https://doi.org/10.1038/natrevmats.2016.9>.
- [19] Z. Cao, J. Bu, Z. Zhong, C. Sun, Q. Zhang, J. Wang, S. Chen, X. Xie, Selective hydrogenation of cinnamaldehyde to cinnamyl alcohol over BN-supported Pt catalysts at room temperature, *Appl. Catal. Gen.* 578 (2019) 105–115, <https://doi.org/10.1016/j.apcata.2019.04.006>.
- [20] A.M. Kovalskii, A.T. Matveev, Z.I. Popov, I.N. Volkov, E.V. Sukhanova, A. A. Lytkina, A.B. Yaroslavtsev, A.S. Konopatsky, D.V. Leybo, A.V. Bondarev, I. V. Shchetinin, K.L. Firestein, D.V. Shtansky, D.V. Golberg, (Ni,Cu)/hexagonal BN nanohybrids – New efficient catalysts for methanol steam reforming and carbon monoxide oxidation, *Chem. Eng. J.* 395 (2020), 125109, <https://doi.org/10.1016/jcej.2020.125109>.
- [21] A.S. Konopatsky, K.L. Firestein, D.V. Leybo, E.V. Sukhanova, Z.I. Popov, X. Fang, A. M. Manakhov, A.M. Kovalskii, A.T. Matveev, D.V. Shtansky, D.V. Golberg, Structural evolution of Ag/BN hybrids via a polyol-assisted fabrication process and their catalytic activity in CO oxidation, *Catal. Sci. Technol.* 9 (2019) 6460–6470, <https://doi.org/10.1039/C9CY01464K>.
- [22] A. Lyalin, A. Nakayama, K. Uosaki, T. Taketsugu, Adsorption and catalytic activation of the molecular oxygen on the metal supported h-BN, *Top. Catal.* 57 (2014) 1032–1041, <https://doi.org/10.1007/s11244-014-0267-7>.
- [23] Y. Cao, P. Maitarad, M. Gao, T. Taketsugu, H. Li, T. Yan, L. Shi, D. Zhang, Defect-induced efficient dry reforming of methane over two-dimensional Ni/h-boron nitride nanosheet catalysts, *Appl. Catal. B Environ.* 238 (2018) 51–60, <https://doi.org/10.1016/j.apcatb.2018.07.001>.
- [24] S.-E. Fu, C.-H. Yeh, P.-J. Lin, S. Nachimuthu, J.-C. Jiang, A first principles study of CO oxidation over gold clusters: The catalytic role of boron nitride support and water, *Mol. Catal.* 471 (2019) 44–53, <https://doi.org/10.1016/j.mcat.2019.04.015>.
- [25] J.T. Grant, C.A. Carrero, F. Goeltl, J. Venegas, P. Mueller, S.P. Burt, S.E. Specht, W. P. McDermott, A. Chieregato, I. Hermans, Selective oxidative dehydrogenation of propane to propene using boron nitride catalysts, *Science* 354 (2016) 1570–1573, <https://doi.org/10.1126/science.aaf7885>.
- [26] R. Huang, B. Zhang, J. Wang, K.-H. Wu, W. Shi, Y. Zhang, Y. Liu, A. Zheng, R. Schlögl, D.S. Su, Direct insight into ethane oxidative dehydrogenation over boron nitrides, *ChemCatChem* 9 (2017) 3293–3297, <https://doi.org/10.1002/cctc.20170025>.
- [27] Y.S. Al-Hamdan, D. Alfe, O.A. von Lilienfeld, A. Michaelides, Tuning dissociation using iso-electronically doped graphene and hexagonal boron nitride: Water and other small molecules, *J. Chem. Phys.* 144 (2016), 154706, <https://doi.org/10.1063/1.4945783>.
- [28] C. Megias-Sayago, J.L. Santos, F. Ammari, M. Chenouf, S. Ivanova, M.A. Centeno, J. A. Odriozola, Influence of gold particle size in Au/C catalysts for base-free oxidation of glucose (doi.org/), *Catal. Today* 306 (2018) 183–190, <https://doi.org/10.1016/j.cattod.2017.01.007>.
- [29] A.A. Davydov, Molecular Spectroscopy of Oxide Catalyst Surfaces (doi.org/), Wiley Intersci. Publ. 121 (2003) 466, <https://doi.org/10.1002/0470867981>.
- [30] K.I. Hadjiivanov, G.N. Vayssilov, Characterization of oxide surfaces and zeolites by carbon monoxide as an IR probe molecule (doi.org/), *Adv. Catal.* 47 (2002) 307–511, [https://doi.org/10.1016/S0360-0564\(02\)47008-3](https://doi.org/10.1016/S0360-0564(02)47008-3).
- [31] G. Kresse, J. Furthmüller, Efficient iterative schemes for ab initio total-energy calculations using a plane-wave basis set, *Phys. Rev. B* 54 (1996) 11169–11186, <https://doi.org/10.1103/PhysRevB.54.11169>.
- [32] G. Kresse, D. Joubert, From ultrasoft pseudopotentials to the projector augmented-wave method, *Phys. Rev. B* 59 (1999) 1758–1775, <https://doi.org/10.1103/PhysRevB.59.1758>.

- [33] J.P. Perdew, K. Burke, M. Ernzerhof, Generalized gradient approximation made simple, *Phys. Rev. Lett.* 77 (1996) 3865–3868, <https://doi.org/10.1103/PhysRevLett.77.3865>.
- [34] S. Grimme, J. Antony, S. Ehrlich, H. Krieg, A consistent and accurate ab initio parametrization of density functional dispersion correction (DFT-D) for the 94 elements H–Pu, *J. Chem. Phys.* 132 (2010), 154104, <https://doi.org/10.1063/1.3382344>.
- [35] R. Geick, C.H. Perry, G. Rupprecht, Normal modes in hexagonal boron nitride, *Phys. Rev.* 146 (1966) 543–547, <https://doi.org/10.1103/PhysRev.146.543>.
- [36] D.V. Shtansky, O. Tsuda, Y. Ikuhara, T. Yoshida, Crystallography and structural evolution of cubic boron nitride films during bias sputter deposition, *Acta Mater.* 48 (2000) 3745–3759, [https://doi.org/10.1016/S1359-6454\(00\)00159-2](https://doi.org/10.1016/S1359-6454(00)00159-2).
- [37] D.K. Singh, P.K. Iyer, P.K. Giri, Diameter dependence of interwall separation and strain in multiwalled carbonnanotubes probed by X-ray diffraction and Raman scattering studies, *Diam. Relat. Mater.* 19 (2010) 1281–1288, <https://doi.org/10.1016/j.diamond.2010.06.003>.
- [38] L. Bergman, R.J. Nemanich, Raman spectroscopy for characterization of hard, wide-bandgap semiconductors: diamond, GaN, GaAlN, AlN, BN, *Annu. Rev. Mater. Sci.* 26 (1996) 551–579, <https://doi.org/10.1146/annurev.ms.26.080196.003003>.
- [39] R.V. Gorbachev, I. Riaz, R.R. Nair, R. Jalil, L. Britnell, B.D. Belle, E.W. Hill, K. S. Novoselov, K. Watanabe, T. Taniguchi, Hunting for monolayer Boron Nitride: optical and Raman signatures, *Small* 7 (2011) 465–468, <https://doi.org/10.1002/smll.201001628>.
- [40] C. Casiraghi, S. Pisana, K.S. Novoselov, A.K. Geim, A.C. Ferrari, Raman fingerprint of charged impurities in graphene, *Appl. Phys. Lett.* 91 (2007), 233108, <https://doi.org/10.1063/1.2818692>.
- [41] B. Zhong, T. Zhang, X.X. Huang, G.W. Wen, J.W. Chen, C.J. Wang, Y.D. Huang, Fabrication and Raman scattering behavior of novel turbostratic BN thin films, *Mater. Lett.* 151 (2015) 130–133, <https://doi.org/10.1016/j.matlet.2015.03.059>.
- [42] Cedric Powell, X-ray photoelectron spectroscopy database XPS, Version 4.1, NIST Stand. Ref. Database 20 (1989), <https://doi.org/10.18434/T4T88K>.
- [43] K. Liu, A. Wang, T. Zhang, Recent advances in preferential oxidation of CO reaction over platinum group metal catalysts, *ACS Catal.* 2 (2012) 1165–1178, <https://doi.org/10.1021/cs200418w>.
- [44] R.A. Olsen, G.J. Kroes, E.J. Baerends, Atomic and molecular hydrogen interacting with Pt(111), *J. Chem. Phys.* 111 (1999) 11155–11163, <https://doi.org/10.1063/1.480473>.
- [45] M. Gao, A. Lyalin, T. Taketsugu, Oxygen activation and dissociation on h-BN supported Au atoms, *Int. J. Quant. Chem.* 113 (2013) 443–452, <https://doi.org/10.1002/qua.24066>.
- [46] K. Mao, W. Zhang, Y. Pei, X.C. Zeng, X. Wu, J. Yang, A theoretical study of single-atom catalysis of CO oxidation using Au embedded 2D h-BN monolayer: A CO-promoted O<sub>2</sub> activation, *Sci. Rep.* 4 (2014) 5441, <https://doi.org/10.1038/srep05441>.
- [47] S. Lin, X. Ye, R.S. Johnson, H. Guo, First-principles investigations of metal (Cu, Ag, Au, Pt, Rh, Pd, Fe, Co, and Ir) doped hexagonal boron nitride nanosheets: stability and catalysis of CO oxidation, *J. Phys. Chem. C.* 117 (33) (2013) 17319–17326, <https://doi.org/10.1021/jp4055445>.
- [48] X. Liu, T. Duan, C. Meng, Y. Han, Pt atoms stabilized on hexagonal boron nitride as efficient single-atom catalysts for CO oxidation: a first-principles investigation, *RSC Adv.* 5 (2015) 10452–10459, <https://doi.org/10.1039/C4RA14482A>.
- [49] R.S. Singh, R.Y. Tay, W.L. Chow, S.H. Tsang, C. Mallick, E.H. Teo, Band gap effects of hexagonal boron nitride using oxygen plasma, *Appl. Phys. Lett.* 104 (2014), 163101, <https://doi.org/10.1063/1.4872318>.
- [50] M. Haruta, Catalysis of gold nanoparticles deposited on metal oxides, *CATTECH* 6 (2002) 102–115, <https://doi.org/10.1023/A:1020181423055>.
- [51] M. Haruta, When gold is not noble: catalysis by nanoparticles, *Chem. Rec.* 3 (2003) 75–87, <https://doi.org/10.1002/tcr.10053>.
- [52] M. Haruta, S. Tsubota, T. Kobayashi, H. Kageyama, M.J. Genet, B.J. Delmon, Low-Temperature Oxidation of CO over Gold Supported on TiO<sub>2</sub>,  $\alpha$ -Fe<sub>2</sub>O<sub>3</sub>, and Co<sub>3</sub>O<sub>4</sub>, *Catal.* 144 (1993) 175–192, <https://doi.org/10.1006/jcat.1993.1322>.
- [53] T.-M. Tran-Thuy, C.-C. Chen, S.D. Lin, Spectroscopic studies of how moisture enhances CO oxidation over Au/BN at ambient temperature, *ACS Catal.* 7 (7) (2017) 4304–4312, <https://doi.org/10.1021/acscatal.7b01374>.
- [54] M. Sun, Q. Fu, L. Gao, Y. Zheng, Y. Li, M. Chen, X. Bao, Catalysis under shell: Improved CO oxidation reaction confined in Pt@h-BN core–shell nanoreactors, *Catal. Shell: Improv. CO Oxid. React. Confin. Pt@H -BN core–Shell nanoreactors* 10 (2017) 1403–1412, <https://doi.org/10.1007/s12274-017-1512-8>.
- [55] S.J. Tauster, S.C. Fung, R.L. Garten, Strong metal-support interactions. Group 8 noble metals supported on TiO<sub>2</sub> (doi.org/), *J. Am. Chem. Soc.* 100 (1) (1978) 170–175, <https://doi.org/10.1021/ja00469a029>.
- [56] T. Song, J. Dong, R. Li, X. Xu, M. Hiroaki, B. Yang, R. Zhang, Y. Bai, H. Xin, L. Lin, R. Mu, Q. Fu, X. Bao, Oxidative strong metal-support interactions between metals and inert boron nitride (doi.org/), *J. Phys. Chem. Lett.* 12 (2021) 4187–4194, <https://doi.org/10.1021/acs.jpclett.1c00934>.
- [57] Q. Wang, Q. Zhang, X. Zhao, X. Luo, C.P.Y. Wong, J. Wang, D. Wan, T. Venkatesan, S.J. Pennycook, K.P. Loh, G. Eda, A.T.S. Wee, Point defects in two-dimensional hexagonal boron nitride: A perspective, *Nano Lett.* 18 (2018) 6898–6905, <https://doi.org/10.1063/5.0021093>.
- [58] M.D. Esrafili, N. Saeidi, P. Nematiollahi, The healing of B- or N-vacancy defective BNNTs by using CO molecule: a DFT study, *N. J. Chem.* 40 (2016) 8024–8031, <https://doi.org/10.1039/C6NJ00921B>.
- [59] L. Zhang, I.A.W. Filot, Y.-Q. Su, J.-X. Liu, E.J.M. Hensen, Understanding the impact of defects on catalytic CO oxidation of LaFeO<sub>3</sub>-supported Rh, Pd, and Pt single-atom catalysts, *J. Phys. Chem. C.* 123 (2019) 7290–7298, <https://doi.org/10.1021/acs.jpcc.9b01520>.
- [60] C. Meng, Y. Li, H. Wu, W. Wei, Y. Ning, Y. Cui, Q. Fu, X. Bao, Structural transformation of h-BN overlayers on Pt(111) in oxidative atmospheres, *Phys. Chem. Chem. Phys.* 20 (2018) 11013–11020, <https://doi.org/10.1039/C8CP00877A>.
- [61] M. Gao, A. Lyalin, T. Taketsugu, Oxygen activation and dissociation on h-BN supported Au atoms, *Int. J. Quantum Chem.* 113 (2013) 443–452, <https://doi.org/10.1002/qua.24066>.
- [62] M. Gao, A. Lyalin, T. Taketsugu, Role of the support effects on the catalytic activity of gold clusters: A density functional theory study, *Catalysts* 1 (2011) 18–39, <https://doi.org/10.3390/catal1010018>.
- [63] S.-E. Fu, C.-H. Yeh, P.-J. Lin, S. Nachimuthu, J.-C. Jiang, A first principles study of CO oxidation over gold clusters: The catalytic role of boron nitride support and water, *Mol. Catal.* 471 (2019) 44–53, <https://doi.org/10.1016/j.mcat.2019.04.015>.
- [64] Y. Ding, F. Torres-Davila, A. Khater, D. Nash, R. Blair, L. Tetard, Defect engineering in boron nitride for catalysis, *MRS Commun.* 8 (2018) 1236–1243, <https://doi.org/10.1557/mrc.2018.113>.
- [65] J. Wu, L. Wang, X. Yang, B. Lv, J. Chen, Support effect of the Fe/BN catalyst on Fischer–Tropsch performances: Role of the surface B–O defect, *Ind. Eng. Chem. Res.* 57 (2018) 2805–2810, <https://doi.org/10.1021/acs.iecr.7b04864>.
- [66] W.H. Weinberg, Eley–Rideal surface chemistry: direct reactivity of gas phase atomic hydrogen with adsorbed species, *Acc. Chem. Res.* 29 (10) (1996) 479–487, <https://doi.org/10.1021/ar9500980>.
- [67] W. Zhu, Z. Wu, G.S. Foo, X. Gao, M. Zhou, B. Liu, G.M. Veith, P. Wu, K.L. Browning, H.N. Lee, H. Li, S. Dai, H. Zhu, Taming interfacial electronic properties of platinum nanoparticles on vacancy-abundant boron nitride nanosheets for enhanced catalysis, *Nat. Comm.* 8 (2017) 15291, <https://doi.org/10.1038/ncomms15291>.
- [68] W. Wang, S. Wang, X. Ma, J. Gong, Recent advances in catalytic hydrogenation of carbon dioxide, *Chem. Soc. Rev.* 40 (2011) 3703–3727, <https://doi.org/10.1039/C1CS15008A>.
- [69] H. Yang, C. Zhang, P. Gao, H. Wang, X. Li, L. Zhong, W. Wei, Y. Sun, A review of the catalytic hydrogenation of carbon dioxide into value-added hydrocarbons, *Catal. Sci. Technol.* 7 (2017) 4580–4598, <https://doi.org/10.1039/C7CY01403A>.
- [70] S. Saeidi, S. Najari, F. Faziolahai, M.K. Nikoo, F. Sefidkon, J.J. Klemes, L.L. Baxter, Mechanisms and kinetics of CO<sub>2</sub> hydrogenation to value-added products: A detailed review on current status and future trends, *Renew. Sustain. Energy Rev.* 80 (2017) 1292–1311, <https://doi.org/10.1016/j.rser.2017.05.204>.
- [71] S. Saeidi, N.A.S. Amin, M.R. Rahimpour, Hydrogenation of CO<sub>2</sub> to value-added products—A review and potential future developments, *J. CO<sub>2</sub> Util.* 5 (2014) 66–81, <https://doi.org/10.1016/j.jcou.2013.12.005>.
- [72] J. Kirchner, Z. Baysal, S. Kureti, Activity and structural changes of Fe-based catalysts during CO<sub>2</sub> hydrogenation towards CH<sub>4</sub> – A mini review, *ChemCatChem* 12 (2020) 981–988, <https://doi.org/10.1002/cctc.201901956>.
- [73] M. Fan, J.D. Jimenez, S.N. Shirodkar, J. Wu, S. Chen, L. Song, M.M. Royko, J. Zhang, H. Guo, J. Cui, K. Zuo, W. Wang, C. Zhang, F. Yuan, R. Vajtai, J. Qian, J. Yang, B.I. Yakobson, J.M. Tour, J. Lauterbach, D. Sun, P.M. Ajayan, Atomic Ru immobilized on porous h-BN through simple vacuum filtration for highly active and selective CO<sub>2</sub> methanation, *ACS Catal.* 9 (2019) 10077–10086, <https://doi.org/10.1021/acscatal.9b02197>.
- [74] A. Goguet, F.C. Meunier, D. Tibiletti, J.P. Breen, R. Burch, Spectrokinetic investigation of reverse water-gas-shift reaction intermediates over a Pt/CeO<sub>2</sub> catalyst, *J. Phys. Chem. B.* 108 (2004) 20240–20246, <https://doi.org/10.1021/jp047242w>.
- [75] D. Ferri, T. Bürgi, A. Baiker, Probing boundary sites on a Pt/Al<sub>2</sub>O<sub>3</sub> model catalyst by CO<sub>2</sub> hydrogenation and in situ ATR-IR spectroscopy of catalytic solid–liquid interfaces, *Phys. Chem. Chem. Phys.* 4 (2002) 2667–2672, <https://doi.org/10.1039/B111498K>.
- [76] X. Chen, X. Su, H. Duan, B. Liang, Y. Huang, T. Zhang, Catalytic performance of the Pt/TiO<sub>2</sub> catalysts in reverse water gas shift reaction: Controlled product selectivity and a mechanism study, *Catal. Today* 281 (2017) 312–318, <https://doi.org/10.1016/j.cattod.2016.03.020>.